Clever Ubiagege

Hybrid Additive Manufacturing with MIG-Deposit of Aluminium Alloy Enhanced by Friction Stir Processing

School of Engineering

Thesis submitted for examination for the degree of Master of Science in Technology

Espoo 28.5.2017

Thesis supervisor:

Prof. Pedro Vilaça

ABSTRACT

Author	Clever Ubiagege
Thesis Title	Hybrid additive manufacturing with MIG deposit of aluminium alloy enhanced by friction stir processing
Degree Programme	Mechanical Engineering
Professorship	Product Development and Mechatronics
Thesis Supervisor	Prof. Pedro Vilaça
Date: 28.05.2017	**Number of Pages**: 10+81 **Language**: English

Hybrid additive manufacturing (HAM) is an additive manufacturing (AM) process that integrates multiple metal processing/shaping techniques. This thesis work focuses on the development of a HAM process that combines the MIG welding technique, to produce the initial AM via multi-layer deposit, with friction stir processing (FSP) technique, to enhance the properties of the deposited layers. In order to validate this hybrid concept, filler wire of aluminium alloy AA5183, with diameter of 1.2 mm was deposited on a base plate of aluminium alloy AA5083, with thickness of 6 mm. The initial AM component was produced with three overlapped layers, resulting in a plate of about 400 x 130 x 9 mm, over the base plate. Each layer was produced with parallel and partially overlapping string passes with MIG. The resulting AM component was then processed by FSP, in parallel passes aligned with the initial MIG passes. The effect of the HAM process on the strength and microstructure of the final component was then investigated. It was observed that the initial AM microstructure was refined, with evident dynamic recrystallization in the stirred region by the probe of the FSP tool. There are evidences that the porosities produced by MIG were removed by the FSP. In terms of mechanical properties, the ductility increased in comparison to the initial AM material, in both transversal and longitudinal directions. Concerning the strength, the ultimate tensile (UTS) and yield strength (σ_y) are higher than the initial AM material in the longitudinal direction, but lower than the initial AM material in the transversal direction. This fact is mainly due to the overlap ratio between the FSP passes, along the transversal direction, which did not reach continuous overlapping of the stirred zones. Based on a global analysis, encompassing several mechanical properties, the overall quality of the HAM sample improved in comparison to the initial AM.

Keywords: Metal-based additive manufacturing, Arc-based additive manufacturing, Hybrid additive manufacturing, Friction stir processing, MIG.

AKNOWLEDGEMENTS

I would like to take this opportunity to appreciate my supervisor, Prof. Pedro Vilaça for all his effort and motivation in making this thesis a realization.

Special thanks to Mikko Peltonen and Kim Widell, for the key role that they played during the experimental and testing phase of this work. In addition, I appreciate the contributions rendered by the other workshop and laboratory staff during this work.

I thank the fellow researchers in our office that have been of great assistance in one way or another during these past months.

Finally, my sincere gratitude goes to my parents, family and friends, for their financial support, words of encouragement, and prayers.

Otaniemi, May 28, 2017

Clever Ubiagege

TABLE OF CONTENTS

ABSTRACT i

AKNOWLEDGEMENTS ii

ABBREVIATIONS v

SYMBOLS vi

LIST OF FIGURES vii

LIST OF TABLES ix

1 INTRODUCTION 1

1.1 Objectives 1

1.2 Scope of Thesis 2

1.3 Structure of Thesis 3

2 LITERATURE REVIEW 4

2.1 Printing systems for additive manufacturing 6

2.1.1 Powder-bed system 6

2.1.2 Powder-fed system 7

2.1.3 Wire-fed system 7

2.1.4 Friction stir additive manufacturing (FSAM) 8

2.1.5 Friction surfacing (FS) 10

2.2 Printing processes for metal-based additive manufacturing 11

2.2.1 Laser based 11

2.2.2 Electron based 12

2.2.3 Arc based 12

2.3 Hybrid additive manufacturing (HAM) 14

2.3.1 Robotic MAG and micro-rolling HAM 16

2.3.2 Robotic MAG and metamorphic rolling mechanism HAM 16

2.3.3 Robotic MAG and micro-milling HAM 17

2.4 Friction stir processing (FSP) 19

3 MATERIALS AND METHODS 21

3.1 Robotic weld equipment setup 21

3.2 Friction stir processing setup 23

3.2.1 FSP Tool 24

3.3 Selection of HAM materials 26

3.3.1 AA5XXX Aluminium Alloys 26

3.3.2 Filler Wire 27
3.3.3 Base Plate 28
4 IMPLEMENTATION OF HAM PROCESS 29
4.1 Designing Samples 30
4.2 MIG welding procedure 31
4.2.1 Setting Weld Deposition Parameters 31
4.2.2 Developing the MIG welding paths parameters 31
4.2.3 Building Sample 1 33
4.2.4 Building Sample 2 35
4.3 Friction stir processing procedure 36
4.3.1 Developing the FSP paths parameters 36
4.3.2 FSP of Sample 1 38
4.4 Probe Failure 40
5 TESTING PROCEDURE 44
5.1 Specimen extraction plan 44
5.2 Optical macroscopic and microscopic testing 45
5.3 Microindentation hardness testing 47
5.4 Tensile testing 48
5.5 Bending testing 49
6 RESULTS AND DISCUSSION 51
6.1 Metallurgical analysis 51
6.1.1 Macrostructure Analysis 51
6.1.2 Microstructural Analysis 53
6.2 Microindentation hardness behavior 57
6.3 Tensile behavior 59
6.2.1 Results for AA5183 Al alloy Under Tensile Loading 62
6.2.2 Global efficiency analysis: GETS 63
6.4 Bending behavior 65
6.3.1 Results for AA5183 Al alloy Under Bending Test 66
6.3.2 Global efficiency analysis: GEB 67
7 Final Remarks 69
7.1 Conclusions 70
7.2 Future developments 70
REFERENCE 72
ANNEX 76

ABBREVIATIONS

AM	Additive Manufacturing
CAD	Computer Aided Design
MIG	Metal Inert Gas
MAG	Metal Arc Gas
EBM	Electron Beam Melting
DED	Direct Energy Deposition
SLMS	Selective Laser Metal Sintering
SLM	Selective Laser Melting
SLS	Selective Laser Sintering
LMD	Laser Metal Deposition
FSAM	Friction Stirred Additive Manufacturing
FSW	Friction Stir Welding
FSP	Friction Stir Processing
FS	Friction Surfacing
HAM	Hybrid Additive Manufacturing
HDMR	Hybrid Deposition and micro-Rolling
MRM	Metamorphic Rolling Mechanism
SDM	Shape Deposition Manufacturing
CMB	Controlled Material Build-up
IPT	Institute for Production Technology
UTS	Ultimate Tensile Strength
A	Elongation
T	Tensile specimen from As-Welded Sample
T_HAM	Tensile Specimen from HAM sample
B	Bending test Specimen from As-Welded Sample
B_HAM	Bending Specimen from HAM sample
GETS	Global Efficiency Tensile Strength
GEB	Global Efficiency Bending
SZ	Stirred zone

HAZ	Heat affected zone
TMAZ	Thermo-mechanically affected zone
EBSD	Electron Back-Scatter Diffraction

SYMBOLS

ε	True Strain
e	Nominal Strain
σ	Nominal Stress
S	True Stress
l_0	Original length of tensile specimen
K	Stiffness
A_0	Cross sectional Area
J_p	Polar moment of area
I	Moment of inertia
M	Bending Moment
T_s	Spindle Torque
Ω	Tool rotation
v	Travel speed
E	Young Modulus
F_B	Bending Force
U	Toughness or Energy
A	Elongation
σ_y	Yield Strength
$\int$	Integral

LIST OF FIGURES

Figure 1: Historical development of meta-based AM processes [1].....4
Figure 2: Powder-bed System [8].....6
Figure 3: Typical setup of powder-fed system [8].....7
Figure 4: WIre-fed system [8].....7
Figure 5: Friction stir additive manufacturing technique [9].....8
Figure 6: (a) Macrograph of an AA5083 alloy fabricated using FSAM at 500 rpm and 152 mm/min. Hardness profile along the build direction in the as-built condition. (c) A comparison between the uniaxial tensile stress–strain curves in AA5083-O temper and built stack [9].....9
Figure 7: Friction surfacing technique [13].....10
Figure 8: Schematics of Laser-based AM setup [56].....11
Figure 9: Electric arc-based AM Equipment [55].....13
Figure 10: Strength and ductility achieved by the fusion-based additive techniques compared with the base material for different alloys [9].....14
Figure 11: Robotic MAG and micro-rolling process [34].....16
Figure 12: Robotic MAG and MRM process [31].....17
Figure 13: Robotic MAG and Micro-milling technique [36].....18
Figure 14: Schematic representation of stacked alloy sheets [41].....19
Figure 15: SEM/BEI micrographs of the Mg70Al15Zn15 system after two and three passes (a) and (b), and the Mg60 Al20Zn20 system after two and three passes (c) and (d) [41].....20
Figure 16: The variation of H_v along the transverse cross-sectional plane [41].....20
Figure 17: Robotic MIG AM Equipment.....22
Figure 18: FSP Machine and Tool.....24
Figure 19: Selected Probe and Shoulder.....26
Figure 20: Robotic MAG and friction stirring process.....29
Figure 21: Weld Bead Geometry.....30
Figure 22: Sample 1 Weld Deposit.....35
Figure 23: Sample 2 Weld Deposit.....36
Figure 24: FSP of Sample 1.....40
Figure 25: Fractured Probes.....41
Figure 26: Generated Forces from FSP.....41
Figure 27: Processing region of probe.....43
Figure 28: Specimen Extraction Model for Sample 2.....44
Figure 29: Specimen Extraction Model for Sample 1.....45
Figure 30: Equipment setup for Optical macrostructural and microstructural observation.....46
Figure 31: Specimens from As-MIG-welded and HAM samples for Metallurgy Analysis.....46
Figure 32: Linear patterned hardness profile.....48
Figure 33: Tensile Test Specimens.....49
Figure 34: Bending Test Specimens.....50
Figure 35: Optical Macrograph of As-MIG-welded workpiece (sample 2).....52
Figure 36: Optical Macrograph of FSP workpiece (sample 1).....53
Figure 37: Optical micrograph of specimens extracted at specific position of sample 2.....54

Figure 38: Optical micrograph of specimens extracted at specific position of sample 1 54
Figure 39: Particle distribution across specimens under Optical microscope. (a) Particle distribution in sample 2 (as-MIG-welded), (b) Particle distribution in sample 1 (HAM sample). ...55
Figure 40: Boundary between FSP zone and MIG-welded zone under optical microscope 55
Figure 41: MIG-sample hardness contour plot 57
Figure 42: Contour plot of HAM sample 58
Figure 43: Linear plot of MIG and HAM Hardness specimen through section A-A 58
Figure 44: Nominal Stress-Strain of Sample 1 and 2 60
Figure 45: True Stress-Strain of Sample 1 and 2 60
Figure 46: Elastic Region of HAM Specimen (T_HAM3-Longitudinal) 61
Figure 47: Plastic Region of HAM Specimen (T_HAM3-Longitudinal) 61
Figure 48: Relationship between the UTS and Ductility of Sample 1 and 2 63
Figure 49: Static bending test on specimens from Sample 1 and 2 65
Figure 50: Curve fitted function on B_HAM2 specimen 66
Figure 51: Boundary between base plate and MIG-weld beads under optical microscope 76
Figure 52: Elastic Region of T_HAM2 76
Figure 53: Plastic Region of T_HAM2 77
Figure 54: Elastic Region of T_HAM1 77
Figure 55: Plastic Region of T_HAM1 78
Figure 56: Elastic Region of T_MIG5 78
Figure 57: Plastic Region of T_MIG5 79
Figure 58: Elastic Region of T_MIG2 79
Figure 59: Plastic Region of T_MIG2 80
Figure 60: Curve fit function on Force-Displacement of B_MIG1 80
Figure 61: Curve fit function on Force-Displacement of B_MIG2 81
Figure 62: Curve fit function on Force-Displacement of B_HAM1 81

LIST OF TABLES

Table 1: Chemical composition of Filler Wire [46] 27
Table 2: Physical Properties of Filler Wire [47] 27
Table 3: Physical properties and Chemical composition of Base Plate 28
Table 4: Design Samples Dimensions 30
Table 5: Weld beads deposition parameters 31
Table 6: Individual weld path parameters. The nth path is the last weld pass that makes up a complete layer width. 33
Table 7: FSP Parameters 38
Table 8: Microindentation hardness input parameters 47
Table 9: Summary of Mechanical Properties of Specimens under Tensile Loading 62
Table 10: GETS formulation 64
Table 11: Summary of static bending test analysis 67
Table 12: GEB formulation 68

1 INTRODUCTION

Additive manufacturing (AM) is a manufacturing process that involves building of part layer-by-layer on a platform along predefined paths, typically generated from 3D CAD model. Metal-based AM is a part of AM technology that uses metallic material as the base engineering material for manufacturing. Other categories of AM-based processes, can be found categorized in terms of based material, including e.g. polymer, ceramics, concrete, and hybrid materials. AM-based processes can also be found categorized in terms of the power source, where the most common are Laser-based, Electron beam-based and Arc-based.

The parts produced by metal-based AM processes are prone to defects, mainly when dealing with aluminium alloys as base material. These defects limits the transferability of metal-based AM processes to industrial environment and further extent of industrial applications for the built parts. In an attempt to tackle some of these challenges, the hybrid additive manufacturing was introduced. Hybrid additive manufacturing (HAM) in this thesis was applied to aluminium alloy, entailing the combination of MIG process, as a source for the additive deposits, with a solid-state thermomechanical processing technique, the friction stir processing (FSP) process, to heal eventual defects and improve the material properties.

1.1 Objectives

The aim of this thesis is to develop a HAM process for manufacturing sound aluminum alloy components with high strength and toughness by combining MIG welding, as source of metal depositing, and FSP as an improvement technique. The development process is based on the following objectives:

i. To develop experimental conditions for both MIG welding and FSP (focus on the clamping system);
ii. To produce and test the multi-pass MIG welding and layer stacking;
iii. To produce and test the multi-pass FSP over the initial metal deposits;

iv. To establish best set of operational conditions and parameters for HAM (the combined MIG welding and FSP operation);
v. To produce samples for testing and analysis.
vi. To evaluate the material properties.

1.2 Scope of Thesis

In recent years, there has been growing interest in using additive manufacturing (AM) process for fabricating metal parts. However, the fabricated parts usually have low strength and/or toughness in comparison to the bulk base material and they usually take too long to produce, when they are based on sintering processes. In an attempt to reduce the production time, arc-based AM process was introduced. Although the production rate significantly increased, the performance index of the produced parts did not improve when compared to their bulk base materials. The low strength quality of the parts can be attributed to micro-voids across the component, and the thermal cycle at the heat-affected zone (HAZ), where partial to full recrystallization, grain growth and other aging effects exist. Thus, the heat flowing from the heat source onto the material during component fabrication is typically considered as the main factor for the low mechanical strength of metal parts produced, based on fusion additive manufacturing (laser, electron beam or electric arc as heating source). To overcome this issue, several work has been carried out to reduce the influence of HAZ by using solid-state processing techniques in AM of parts. FSAM (an adopt of FSW) as a solid state processing technique has proven to improve the strength of AM parts in comparison to their base materials, as it tends to remove the defects previously mentioned in fusion-based AM processes. By implementing this technique, the HAZ affected zone is drastically reduced while an introduced TMAZ is significantly increased. However, FSAM cannot be used in manufacturing complex or freeform components, thereby limiting the widespread application of AM in the automobile and aeronautic industries.

In this work, a novel HAM process is implemented to produce high strength aluminium alloy by combining MIG welding and FSP. The aluminium alloy AA5183 was used as AM metal and the AA5083 was selected as the base plate. These aluminium alloys were selected

because of their good combination of strength and corrosion resistance. The strength is dependent on work hardening which is suitable for improvement with FSP. In order to evaluate this HAM process, mechanical and metallurgical analysis were carried out on specimens extracted from two parts produced with MIG AM and two parts produced with HAM. To investigate the properties, several test procedures were implemented, such as, tensile test, bending test, hardness test, and metallurgical test. The analysis on the test data reveals some deviation of the mechanical properties between the two parts under comparison, both for MIG welding and FSP. In addition, a global analysis of the mechanical properties was implemented for the HAM concept.

1.3 Structure of Thesis

This thesis is divided into 7 chapters. The current chapter introduced the thesis. Chapter 2 provides an extensive literature review on AM processes. Chapter 3 describes the experimental setup and material selection for HAM implementation. Chapter 4 presents the step-by-step implementation of the HAM process. Chapter 5 describes the plan, conditions and procedures for the experimental tests to evaluate the MIG-based AM and the HAM process. Chapter 6 analyzes the test results and provides elaborated discussions and comments on the results. Chapter 7 reviews the previous chapters, depicting the conclusions and proposing some ideas for future development.

2 LITERATURE REVIEW

The previous chapter presented the motive behind developing a hybrid additive manufacturing (AM) process. This chapter presents a background description of AM process with a focus on metallic material fabrication. Section 2.1 and 2.2 describe the various printing systems and processes in metal-based AM respectively. The state of the art on different hybrid processes is presented in section 2.3. Finally, FSP, which is an adopt of FSW, is described in Section 2.4.

Additive manufacturing can also be referred to as Rapid prototyping or 3D printing. It was first developed in the 80s for rapidly producing prototypes or models to be showcased. The first record on additive manufacturing was in 1987 by 3D systems. They called the process stereolithography; it involves heating thin layers of light sensitive liquid polymers with laser until they solidify . The history of the development of AM specifically metal-based over the years is too enormous to narrate in this thesis. Thus, Figure **1** shows a graphical summary of development of metal-based AM processes [1].

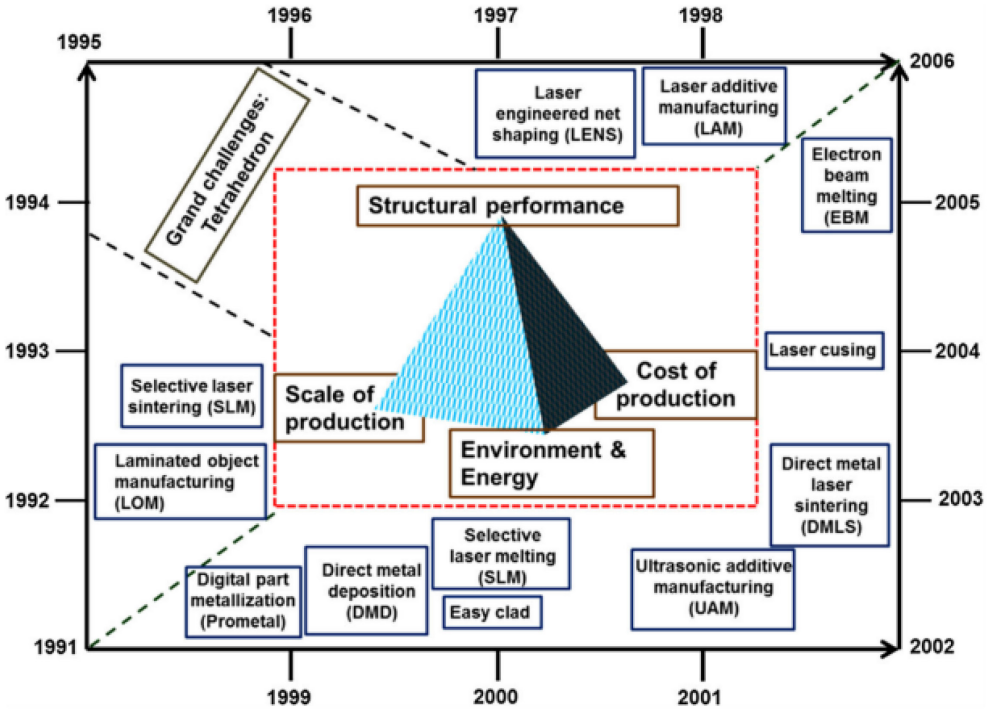

Figure 1: Historical development of meta-based AM processes **[1]**

Fast forward 25 years, AM technology is currently been used to manufacture structural engineering components in addition to model designing and prototyping. These days, AM equipment can be found in homes, schools, offices and industrial places.

Owing to wide acceptance and numerous research work being carried out on of AM technology, the direct end-use application is growing tremendously, from automotive application to aerospace and even ship building applications. This manufacturing process is currently producing high quality parts in terms of, surface finish, geometrical accuracy, and considerable high strength. The growth rate of this sector has been phenomenal that even large companies like Airbus, Boeing and GE have been aggressively investing and researching on further application of AM in their industry [1] [2].

In the past, manufacturing industry could only produce customizable or complex parts by traditional manufacturing processes (like subtractive manufacturing and casting) and the degree of customization or complexity of these produced parts were limited. Casting procedures for low batch production were quite challenging to implement. The major challenges included, down time and high cost in planning, designing, manufacturing, and preparing mold. In addition, subtractive manufacturing process led to wastage of material because of continuous removal of metal-chips from workpiece. However, with the introduction of AM process, the production of complex parts became possible that previously could not be manufactured by either machining, or casting. In addition, AM process made it possible to quickly, and cheaply manufacture low volume units of components in comparison to traditional manufacturing methods.

According to many researchers on AM, there are many challenges affecting the AM industry that needs to be addressed before the forecasted usage growth can be met [3]. The good news is that most of these challenges has opened door to new opportunities. In the event of proposing and providing solutions to these challenges; new printing systems, equipment, materials, different control systems, sensors, monitoring units, algorithms, and simulation, have been developed but as the solutions pool grow, so also new challenges are surfacing.

In a typical metal-based AM machine, there are more than 134 parameters (user-defined and predefined) that are used for controlling the building process of a metallic part [4]. The effective control of these parameters yield a high quality 3D built. If these parameters are not properly handled, large amount of defects are bound to exist in the manufactured part, which

in turn will lead to premature failure of the part [5]. The quality of a product is the most critical factor that affects the design of products for commercial use. The quality of a 3D article can be seen from different perspective like performance, reliability, durability, serviceability, aesthetics, and conformance to standard [3], [5].

2.1 Printing systems for additive manufacturing

Based on the way the 3D prints are built on the platform, metal-based AM system can thus be classified into 3 categories according to ASTM [6] [7]:

2.1.1 Powder-bed system

In this AM system, a desired amount of metal powder is lifted from a reservoir and spread unto the build platform or bed at a time [8]. Heat energy from a laser beam or electron beam head focused on the powder-bed causes the powder to sinter or melt and fuse to one another along a programmed path [1]. After fusion, the bed platform is slightly lowered and the whole process of lifting, spreading, and sintering/melting powder is repeated until the built is complete as shown in Figure **2**.

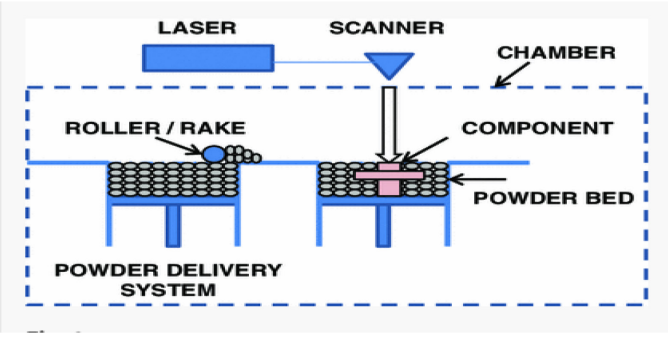

Figure 2: Powder-bed System **[8]**

2.1.2 Powder-fed system

In this AM system, metal powder is fed through a nozzle unto the build platform and heat energy from a laser is simultaneously release to sinter or melt the powder [2] as shown in Figure **3**. The nozzle and the laser are programmed to follow a predefined path from a 3D CAD file [8].

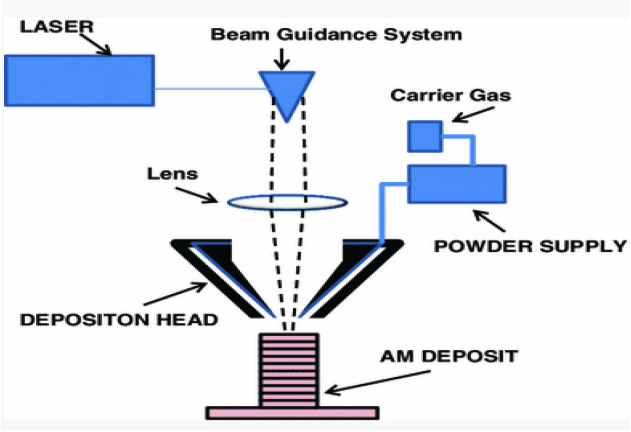

Figure 3: Typical setup of powder-fed system **[8]**

2.1.3 Wire-fed system

In this AM system, metal wire that is fed through a nozzle is melted by a laser beam or electric arc [2], [8]. The molten pool solidifies on a substrate or build platform. Subsequent molten pools are fused layer by layer on previous solid layer in a programmable fashion until a final built is realized. Figure **4** shows a typical arrangement of wire-fed system.

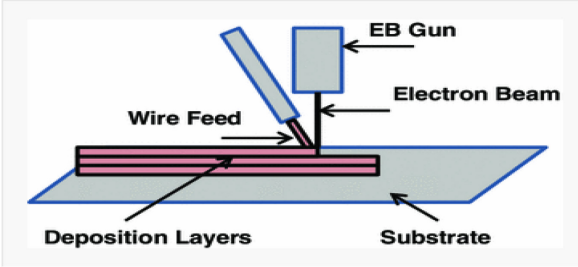

Figure 4: Wire-fed system **[8]**

2.1.4 Friction stir additive manufacturing (FSAM)

In an approach to solve the problem of low mechanical properties of additive manufactured parts in comparison to their base material, the FSAM process was introduced.

FSAM is adopted of friction stir welding process. In FSAM process, a rotary non-consumable insert tool is pressed (exerts an axial force) on sheet of metals that are stack together [9]. The trasverse movement of tool on stack sheets results in the plastic deformation and consolidation of the sheets to form a layer. 3D parts can thus be built layer-by-layer using plastic deformation and consolidation as shown in Figure **5**a.

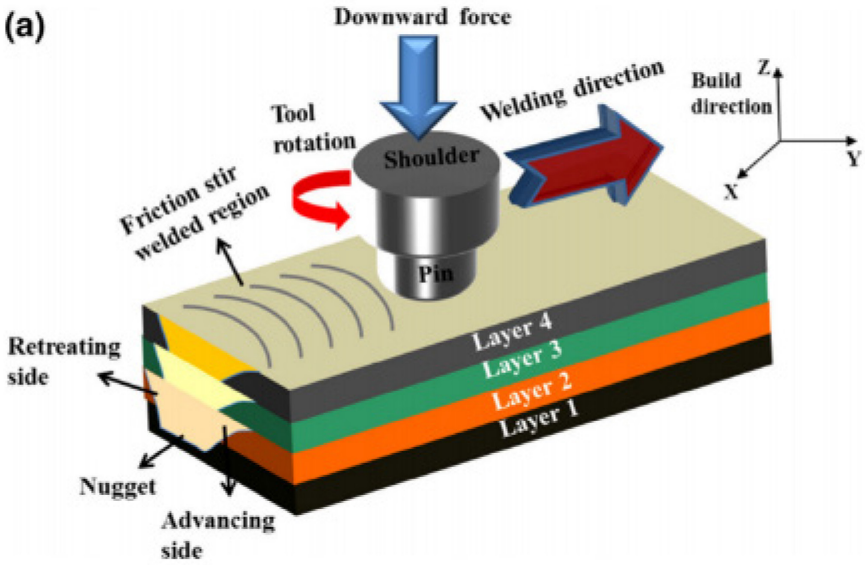

Figure 5: Friction stir additive manufacturing technique **[9]**

In 2006, Airbus and Boeing collaborated in implementing FSAM for the first time in search for ways to produce functional grade parts for the aerospace industry. In that presentation they demonstrated a faster way to fabricate structures with less material waste and prove that functional grade parts can be manufactured with FSAM [9] [10] [11] [12].

Recently, Palanivel et al. [9] also proved that the mechanical properties of additive manufactured parts could be improved by FSAM. In their experimental work with Al alloy, a test of the build showed a yield strength of 267 MPa and ultimate tensile strength (UTS) of

362 MPa after FSAM in comparison to the yield strength and UTS of the base material which are 190 MPa and 336 MPa respectively as shown in Figure **6**[a, b, c].

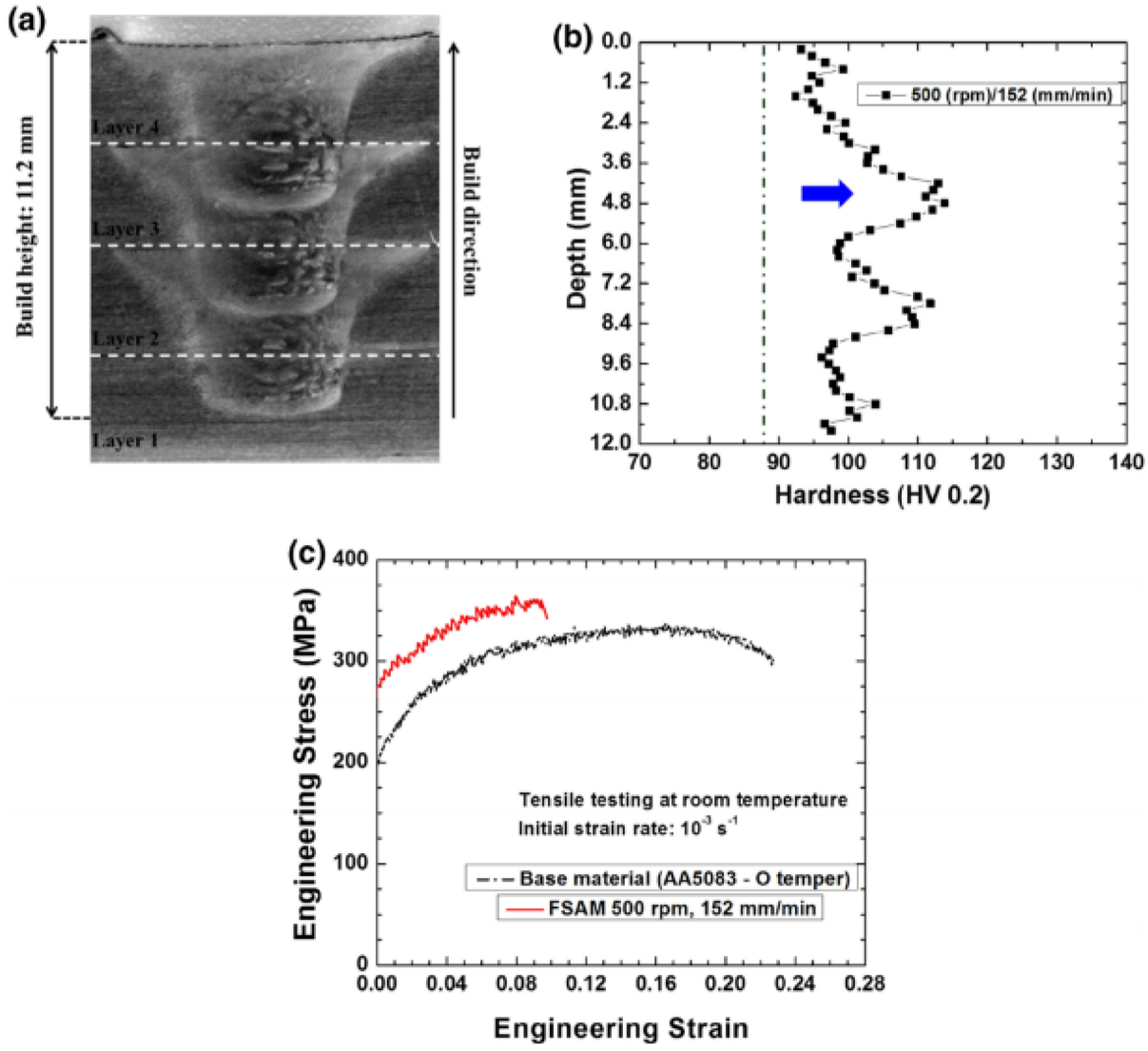

Figure 6: (a) Macrograph of an AA5083 alloy fabricated using FSAM at 500 rpm and 152 mm/min. Hardness profile along the build direction in the as-built condition. (c) A comparison between the uniaxial tensile stress–strain curves in AA5083-O temper and built stack **[9]**.

2.1.5 Friction surfacing (FS)

Friction surfacing is a solid-state coating process that applies plastic deformation phenomenon in depositing and consolidating metal grains from a consumable rod onto a substrate [13]. According to Joao G. [13], FS process involves the pressing of a rotating consumable rod against the surface of a substrate under an applied axial load as shown in Figure **7**.

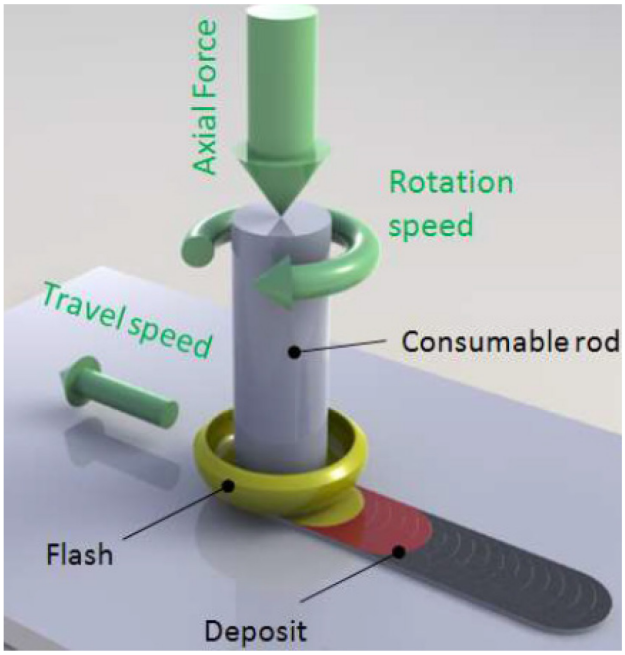

Figure 7: Friction surfacing technique **[13]**

Friction surfacing process has been used in the past for coating metal surfaces to improve the substrate hardness and reduce exposition to environmental degradation (corrosion, wear and fatigue defects that reduces the reliability). It has also been used in repairing cracks and notches on components in other to improve their lifespan.

2.2 Printing processes for metal-based additive manufacturing

AM processes can be broadly classified into three categories based on their energy source; That is, laser based, electron based and arc based [14].

2.2.1 Laser based

In this is additive manufacturing process, a laser is used as the heat or input energy source. The laser beam heats, melts and fuses the powder material onto a substrate. The powder are deposited and fused layer by layer according to a predefined 3D cad model as shown in Figure **8**.

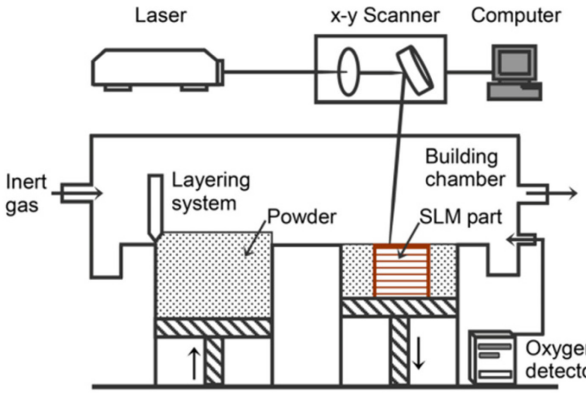

Figure 8: Schematics of Laser-based AM setup [56]

There are different kind of AM processes that use laser beam as the heat source, such as: direct energy deposition (DED), selective laser melting (SLM), selective laser sintering (SLS), laser metal deposition (LMD), etc.

In an SLM process, metallic powder is melted and fused together using laser heat. SLM process was first conceived in 1995 in Fraunhofer Institute ILT Aachen, Germany [15] [16]. With LMD process, functional grade parts can easily be manufactured [17]. It involves jetting metallic power from a nozzle and at same time a focused laser beam moving with the nozzle melts and bonds the powder particles layer by layer along a predefined path.

One of the challenges of this AM process is that, the produced parts usually have high inherent residual stresses and low mechanical properties. This induced residual stresses leads to shrinkage and warpage that eventually causes geometrical inaccuracy [18] [19] [20] [21]. Wei L. et al. [21] studied the effect of laser scanning speed on a Ti-45Al-2Cr-5NB alloy processed by SLMS. They observed that an increase in laser scanning speed from 500 to 800mm/s decreases the grain size from 7.11 μm to 5.43 μm, α_2 phase decreases while the γ and *B_MIG2* phases increase with increasing laser scanning speed. The nano-hardness of TiAl alloy increases from 7.90 ± 0.32 GPa to 9.49 ± 0.46 GPa with increasing laser-scanning speed. The hardness value for the TiAl alloy built under this condition was found to be higher than those manufactured by casting or reinforcement technique.

2.2.2 Electron based

An EBM AM process is similar to laser-based AM, but in this case an electron beam is used as the heating source.

In recent years, both laser based and electron based AM processes for metallic part build have been quite popular in the metal fabrication industry. The ability of using these manufacturing processes to build complex end-use parts with high quality surface finish has been the reason for their attractiveness. The only drawback is their low mechanical properties in comparison with their base material [1] . In a study by Bingjing et al. [20] on properties of Ti-6Al-4V alloy using SLM and EBM, they found out that the microstructure of the built part by SLM and EBM were different. Intermetallic compounds were observed in EBM specimen, and alpha phase and twin crystal were observed in SLM specimen. Corrosion resistance of SLM specimen was better than that of EBM; that is the rate of corrosion for SLM specimen was 2.87 x 10-3mm/a, and EBM was 16.4 x 10-3mm/a under experimental conditions.

2.2.3 Arc based

This AM process is also known as robotic MAG/MIG AM process as depicted in Figure **9**. One of the drawbacks of the arc-based process is that of poor surface finish and thus requires additional tooling.

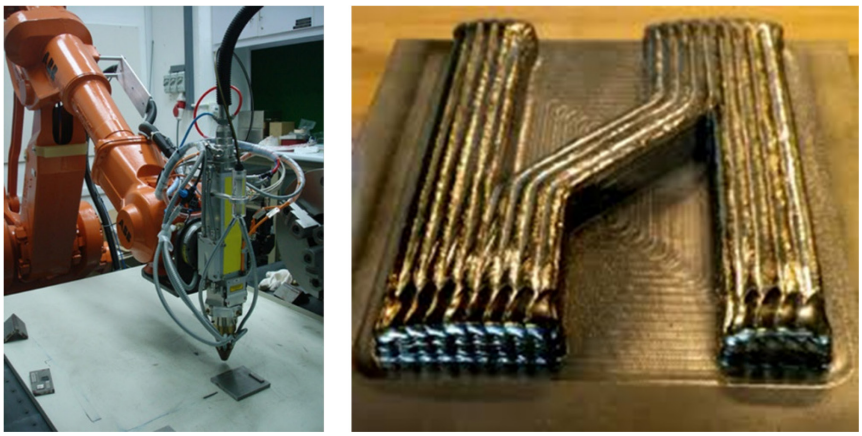

Figure 9: Electric arc-based AM Equipment [55]

According to Takagi et al. [22], direct metal lamination is an AM process that entails the use of robotic MAG welding. In this process, an alloy wire acting as an electrode is fed through a nozzle and is melted with a discharge arc along a predefined path from a 3D CAD model [8]. This technique was first implemented in Germany in the 1960s [23]. They have been used to make large parts and components like pressure vessel of about 500tons, large components made from austenitic material, high performance alloy aircraft engine parts [24] [25] [26] [27].

In recent years, most of the investigation on this process has been on the bead profile and sectional geometry of the weld beads (single-pass and overlapping of adjacent beads). These parameters have critical effect on the mechanical properties and dimensional accuracy of the built part [28] [26]. Cao et al. [29] concluded that bead profile that predominantly determine the geometrical accuracy and quality of metal part during 3D welding process, can be controlled by using a canny operator to formulate the weld mathematical model. In another study on weld bead's and overlap beads, showed that the amount of heat (current and voltage) and speed of welding had great effect on the bead profile and thus mechanical properties [30]; that is the yield strength, ultimate tensile strength and hardness increased with increasing weld speed, and the weld elongation increased with increasing current and voltage. Although many researches have been done to improve the mechanical properties of parts built with laser, electron or arc based process, but the melting and solidification that are carried out in these processes usually lead to phase transformation. The liquid to solid phase

transformation has been studied in the past to be the main cause of defects in metal parts and these defects tend to reduce the mechanical properties of the build part [1]. Hence, the above fusion-based processes have limited application in manufacturing functional grade components that are mainly required in both automotive and aerospace industry.

Most of the fusion-based AM have low mechanical properties as earlier pointed out [14]. According to Palanivel et al. [9] parts manufactured by fusion-based AM have earlier knockdown in properties compared to their base material as shown in Figure **10**.

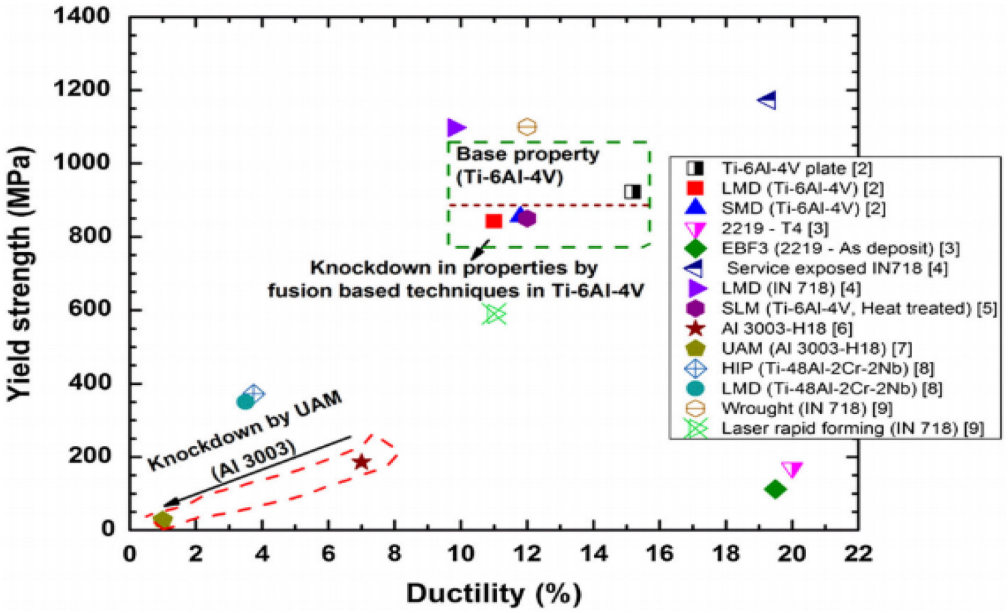

Figure 10: Strength and ductility achieved by the fusion-based additive techniques compared with the base material for different alloys **[9]**

2.3 Hybrid additive manufacturing (HAM)

The HAM is an AM process that combines one of the previously described AM systems with any conventional shaping or joining process. The reason for the hybrid system is to remove some of the bottlenecks that are being experienced by standalone AM processes. Historically, the HAM process was first implemented at the OPM laboratory in Japan were a milling operation was added to an SLS/SLM process [18] [19] [20]. A common problem of this

hybrid system is that metallic powder from the bed can splash on the already machined surface thereby damaging the part [18].

As earlier pointed out that the reason for introducing the HAM was to remove defects from built parts. Defect originate in arc-based AM process mainly because of the liquid-solid phase transformation. The defects introduced by standalone AM processes that have been generally identified by researchers are [31]:

- Poor surface finish.
- Porosity
- Shrinkage (geometrical accuracy)
- Cracking.
- Residual stresses.

The concavity and cross-section of the bead profile in a single-pass or overlapping bead also determine the extent of defects found in a built part. As such, series of attempts have been carried out to control the bead profile of 3D welds in single-pass and overlapped beads but most of the mathematical models and results only improved the surface accuracy and quality of the metal part by small amount. This is because the models could not completely eliminate the concavity caused by inherent surface tension on the beads (molten pool). Techniques and models like multifactor multilevel [32], Taguchi method, Edge detection [28] and statistical and numerical approaches [33], have also been applied to solving these problems but did not yield optimum results. Recent approach to reach the optimum flat bead profile has led to combination of the 3D weld process and thermo -mechanical, mechanical or subtractive technique of flattening the concave bead profile [2]. This is the backbone of the hybrid system [31].

Investigations carried out with hybrid system have shown that the quality of the manufactured parts is greatly improved in comparison to standalone systems.

There is handful of hybrid system for AM process out there but this thesis will be focusing mainly on the arc-based hybrid system. The reason for this is that arc-based AM process is faster and economical; however, there are numerous challenges that still need to be addressed in order to harness its huge potential.

Some of the hybrid systems that are based on integration of MIG/MAG welding and other manufacturing techniques are briefly described in subsequent subsection 2.3.1, 2.3.2, and 2.3.3.

2.3.1 Robotic MAG and micro-rolling HAM

This system combines welding technology and a micro-rolling tool to achieve the desired 3D build. During an HDMR process, a consumable electrode melts and forms beads along a predefined 3D path on a substrate or platform [34]. At the same time, a micro-roller following the MAG nozzle path shapes the weld-beads into desired form as can be observed in Figure **11**. A study on the microstructural evolution of solidification and dynamic recrystallization with this process showed a complete columnar dendritic microstructure. In addition, the rolling reduction area determines the recrystallization region and the size of the recrystallized grains [34].

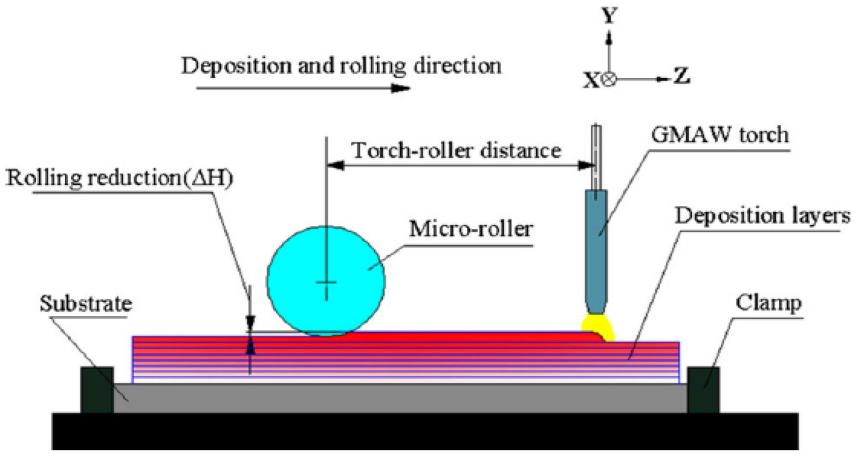

Figure 11: Robotic MAG and micro-rolling process **[34]**

2.3.2 Robotic MAG and metamorphic rolling mechanism HAM

The process is quite similar to HDMR. It comprises of three rollers that form the rolling mechanism as shown in Figure **12**. In this hybrid process, robotic MAG welding is combined with a miniature MRM to help form the desired flat surface on the top and lateral sides of an

overlapping or single-pass bead [31]. The flattening process is achieved by pressing hot rollers against the bead along the welding direction until the bead is plasticized [31]. The plastic deformation is carried out at temperature slightly above the recrystallization temperature [4]. The result shows considerable improvement in both geometrical accuracy and mechanical properties. It was also noted that the improved mechanical properties of the rolled specimen were better than the base material [31]. In addition, columnar grains were observed in the microstructure of the built (tested) part in the vertical direction.

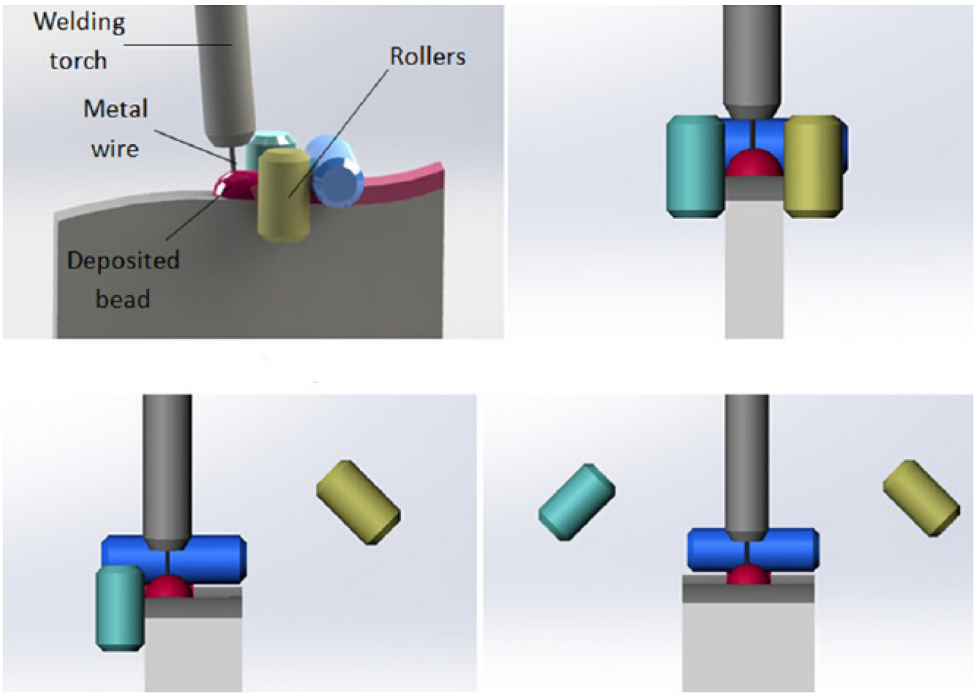

Figure 12: Robotic MAG and MRM process [31]

Colegrove et al. [35] also implemented this hybrid process by using slotted roller (cold rolling technology) to improve the top surface accuracy of the beads. However, this could only be used in linear single-pass beading with the same slot width.

2.3.3 Robotic MAG and micro-milling HAM

This hybrid process was developed to solve the problem of poor surface finish and dimensional accuracy [36]. In this process, robotic MAG welding carries out the AM process

while a micro-milling tool follows the robotic arm to remove concavity on the beads according to predefined 3D path as can be seen in Figure **13**.

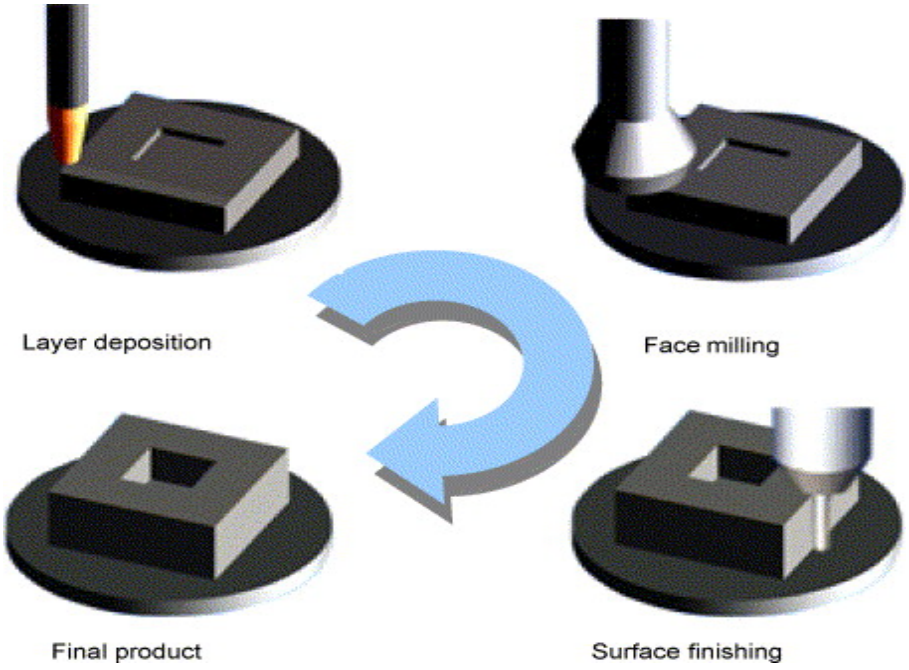

Figure 13: Robotic MAG and Micro-milling technique **[36]**

Combination of additive and subtractive manufacturing has been implemented in Stanford University using the Shape Deposition Manufacturing (SDM) process and in IPT Aachen using Controlled Material Build-Up (CMB) process; both used laser as their heating source [37].

An experimental result on bimetallic parts fabricated by this process shows improved surface quality and dimensional accuracy of the build part. Another advantage of this system is that layer thickness of 0.1-1 mm can be achieved. This process has significant application in building of injection mold inserts, although mechanical properties justification has been neglected [36].

Another drawback of this process is that the part design phase involves trial and error since a cross-section of deposited bead is milled on every layer [38]. In addition, even though the concave surface is successfully removed, there is the issue of increased labor and tooling cost, and reduced material yield [31]- [38] .

2.4 Friction stir processing (FSP)

This is a generic adaptation of FSW, where the tool is traversed along a desired path to modify the microstructure rather than joining two pieces [39]. FSP is a work hardening process, which involves plastic deformation of workpieces along a localized region in order to refine the grains and eliminate defects as the FS tool rotates and travels along the stirred zone (SZ) [40]. In order to obtain fine grain and homogenous microstructure, the traverse speed and tool rotation rate needs to be carefully selected. Ma, Y. [40] observed fine grains with size of ~7.5 μm in the microstructure of a 7075Al-T651 aluminium alloy under a rotating speed of 400 rpm and travel speed of 102 mm/min. In addition, he observed that in some cases when inhomogeneity occurs, the processed zone is still fully recrystallized and fine grains microstructure still exist in the nugget. This leads to better mechanical properties, and improved formability [12] [39] [41] [42] [43] [44] [45].

Chuang et al. [41] studied the effect of FSP on the microstructure and hardness property of MgAlZn alloy by stacking Mg, Al, and Zn foils with thickness of 1, 0.2 and 0.125 mm respectively on one another. The resulting sandwiched structure was held vertically and friction stir processed as shown in Figure **14**.

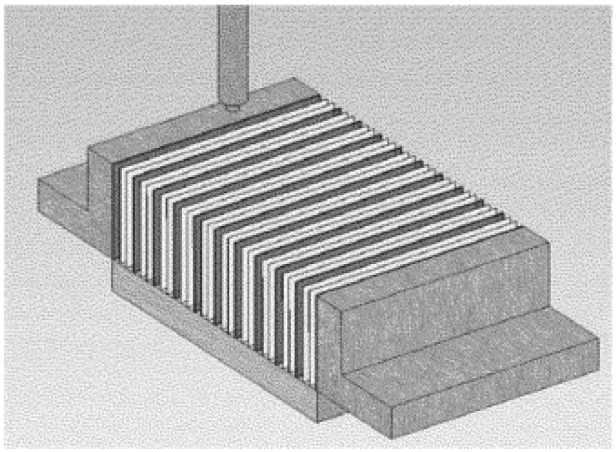

Figure 14: Schematic representation of stacked alloy sheets **[41]**

They observed fine grains and $Mg_3Al_2Zn_3$ phase in the microstructure under a SEM energy dispersive spectrometry. In addition, their observation revealed that as the volume fraction

of the alloying component changes, the amount of darker Mg, lighter Al and white Zn, changes, which clearly indicates phase transformation, as shown in Figure **15**. It was revealed that the hardness value increased with the number of FSP passes and the volume fraction composition of the alloy as shown in Figure **16**(a) and (b).

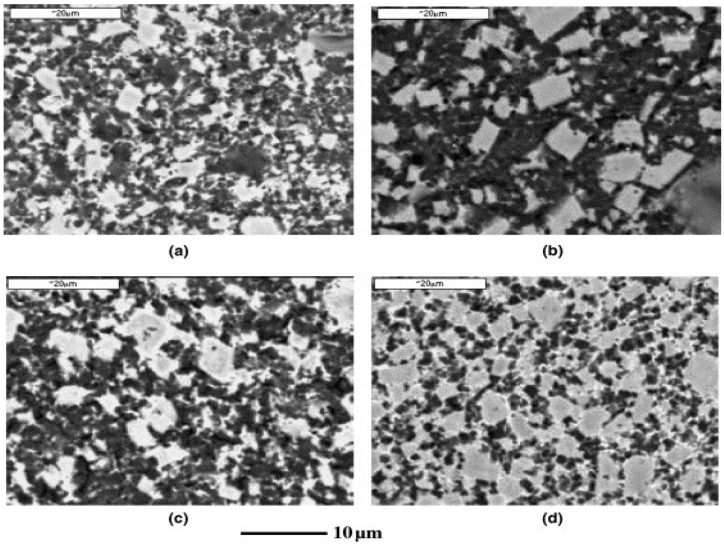

Figure 15: SEM/BEI micrographs of the Mg70Al15Zn15 system after two and three passes (a) and (b), and the Mg60 Al20Zn20 system after two and three passes (c) and (d) **[41]**

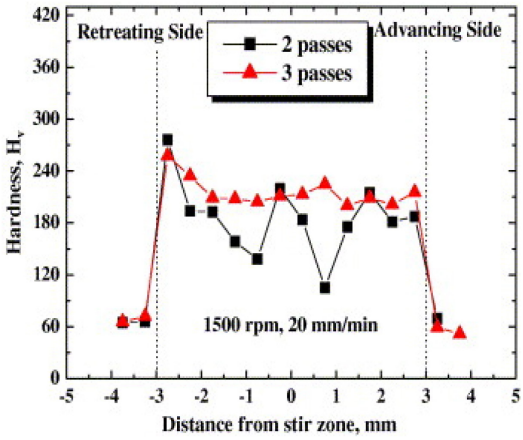

(a) Variation of H_v based on number of passes

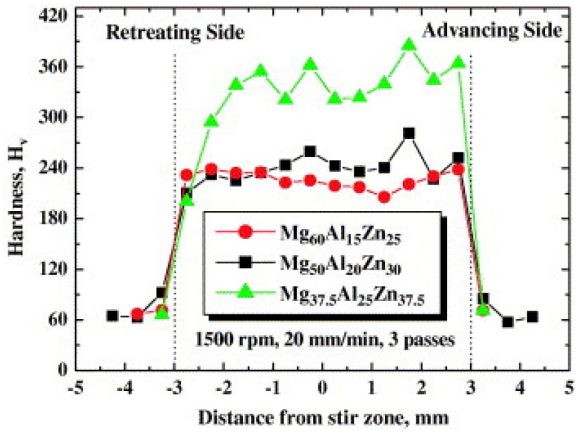

(b) Variation of H_v based on volume fraction

Figure 16: The variation of H_v along the transverse cross-sectional plane **[41]**

3 MATERIALS AND METHODS

The previous chapter provided a framework for theoretical understanding of metal-based AM. This chapter describes the experimental setups, equipment and materials for the proposed hybrid additive manufacturing process.

The conceptual setup of this HAM process comprises of a MIG welding equipment for continuous deposition of weld beads, and a FSW machine for friction stir processing of previously deposited beads.

3.1 Robotic weld equipment setup

Figure **17** shows the various parts of the robotic welding equipment setup. The setup is comprised of a robot, welding touch (D), filler wire, shielding gas, and an ESAB MIG welding equipment (I).

- **Robot:** The robot comprises of a head, two adjustable links, a clamp (for the weld touch) and a bed.
    - **Head:** The head supports the two adjustable links that are hanging freely downwards. It is held in vertical position by a slider mechanism. Its position along the horizontal axis can change across the length of the slider. Accurate change in horizontal position of the head is achieved by a servomotor that is connected to one end of the sliding mechanism, and a control unit. Thus, an operator can change the horizontal position of the head by programmatically setting a travel distance, speed and time, from the control unit.
    - **Adjustable Links:** There are two adjustable links. One is mounted directly on the robotic head and points vertically along the y-axis. The other is mounted horizontally to the vertical link along the z-axis. Each link is connected to a calibration scale and knob to enable manual adjustment of the links along the y and z-axis.

Figure 17: Robotic MIG AM Equipment

A= Head, B= Robot Bed, C= Bed Clamp, D= Weld Touch, E= Robot control panel, F= Adjustable link, G= Knob to adjust link horizontally, H= Knob to adjust link vertically, I= ESAB MIG/MAG welding equipment and J= Welding equipment control panel.

- **Clamp (Weld Touch Holder):** The clamp is mounted to the horizontal adjustable link. It provides a receptacle to hold the weld touch. The clamp can change its position along the x, y and z-axis, and thus, it has 3 degrees of freedom. Its position along x-axis can accurately be changed programmatically from the control unit, whereas its position along the y and z-axis can only be changed manually.

- **Bed:** The robotic arm bed is used for clamping the substrate or plate, on which weld beads are deposited or fabricated. The bed is firmly fixed to the floor; As such, it does not translate nor rotate along any axis.

Other component parts that make up the robotic MIG welding setup includes, welding touch, filler wire holder, shielding gas, and ESAB MIG welding equipment.

3.2 Friction stir processing setup

A typical FSP machine is shown in Figure **18**. The main parts of the FSP machine comprises of the Head, the Bed, Cooling System and Control Panel.

- **The Head:** The head houses a rotating spindle on which various processing and welding tools can be mounted. It can be readily adjustable along x, y, and z-axis over a range of distance; thus, allowing 3-degrees of freedom movement by any tool mounted on the spindle. The head can also be tilted parallel to the x-z plane over a limited angular range, with reference from the z-axis.
- **The Bed:** The bed is firmly fixed to the ground to allow secure clamping of workpieces.
- **Cooling System:** During FSP, considerable amount of heat is generated between the tool and workpiece. As such, the cooling system works to keep the temperature of the tool under a desired level.
- **Control Panel:** This is a computer interface on which welding or processing parameters can be defined. It also houses joysticks through which the processing tool can be moved towards a desired position. It is also equipped with a Start and Reset buttons for initializing and de-initializing a program.

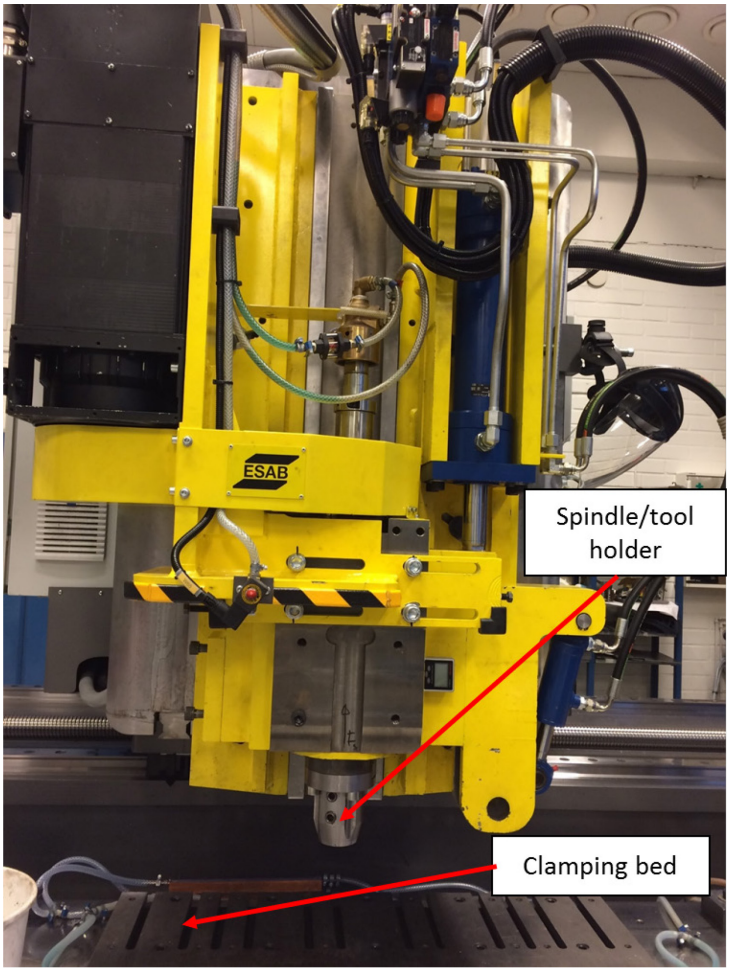

Figure 18: FSP Machine and Tool

3.2.1 FSP Tool

Tool selection:

The tool is made of a probe, shoulder and a tool holder. The tool material needs to fulfill the following requirements:

i. The tool should be able to withstand the forces produced based on the number of layers that need to be processed in a single pass. The strength of the tool must be greater than that of the samples at ambient and processing temperatures

ii. The tool should have high fatigue strength to compensate for multi-pass processing.
iii. High wear resistance at high operating temperatures
iv. Reasonable chemical stability.

Most of the tool for FSW or FSP of 5XXX and 3XXX series aluminium alloys are made of tool steel or high carbon steels that have been properly heat-treated [21]. As such, an H13 tool Steel has been selected as the tool material for friction stir processing of the various samples (AA5183 alloy).

a) **Selecting Probe:** The probe selection is dependent on the workpiece material and the size of the process zone. For the purpose of this experiment, the selected probe was properly sized to process 3 layers of weld beads) at a time such that the processing region of the probe is 9 mm in height and 6 mm in width along its cross-sectional area. In addition, the probe needed to fulfill these requirements:

- The probe should be designed to incorporate truncated conical pin for effective downward material flow during FSP as shown in Figure **19**(b).
- The length of threaded pin should be at least 9mm. The pitch and profile of the thread should also be careful considered to allow for optimum material flow from front side to the backside or trailing side of the pin.
- The probe should fit into a shoulder with inner diameter of 8 mm and tolerance of ± 0.5 mm.
- The probe pin should be able to withstand normal and shear stresses generated during the processing of MIG-welded beads; that is, it should not yield nor fracture.

$$\sigma_0 < \sigma_y$$

b) **Shoulder:** A shoulder was selected with a diameter of 19 mm, and an inner diameter of 8 ± 0.5 mm. The flat surface of the shoulders were modified to concave and slightly chamfered at the edge as shown in Figure **19**(a).

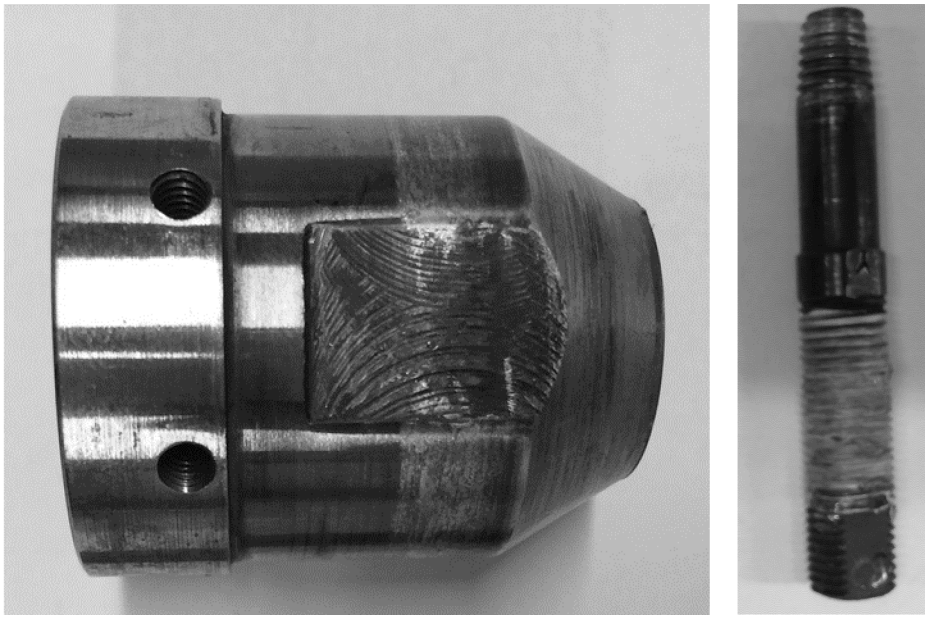

(a) Shoulder (b) Probe

Figure 19: Selected Probe and Shoulder

3.3 Selection of HAM materials

As earlier mentioned, the scope of this thesis has been restricted to metal-based AM process and the material of choice for our experimental work is Aluminium alloy, specifically the 5XXX series alloy. For this experimental work, an aluminium alloy of AA5183 has been selected as the filler material and the substrate on which the weld beads are deposited is of AA5083 aluminium alloy.

3.3.1 AA5XXX Aluminium Alloys

The AA5XXX Al alloys are work-hardening alloys whose mechanical properties can be improved by mechanical straining; their strengthening mechanism is by plastic deformation. They are usually solid-solution hardened by further alloying them with Mg (maximum of 14.9% at 450^0C), but the resulting strength has limitation in certain structural application. As

such, there is need for additional simultaneous work-hardening and annealing in order to further improve the strength. In this thesis work, FSP is used to achieve the simultaneous work-hardening and annealing.

3.3.2 Filler Wire

An AA5183 Al alloy has been chosen for FSP even though fewer works has been done on investigating its behavior during and after FSP or FSW. However, more work has been done with the AA5083 Al alloy, which is in the same family as the AA5183 Al alloy. Thus, it is possible to observe similar metallurgical behavior in both AA5083 and AA5183 Al alloy during and after FSP or FSW.

The chemical composition of the filler wire is shown in Table **1** and physical properties are shown in Table **2**.

Table 1: Chemical composition of Filler Wire [46]

Mg	**Zn**	**Fe**	**Cu**	**Ti**	**Si**	**Mn**	**Al**	**Cr**
4.9%	0.01%	0.13%	0.01%	0.1%	0.04%	0.65%	94.2%	0.08%

Table 2: Physical Properties of Filler Wire **[47]**

Deposition Data	
Diameter	1.2 mm
Current	90 – 210 A
Voltage	15 – 26 V
Tensile Properties (As Welded)	
Yield Strength	125 MPa
Tensile Strength	275 MPa
Elongation	17%

3.3.3 Base Plate

The base plate is the material on which the weld beads (AA5183 Al alloy) are deposited. It is made of AA5083 Al alloy with a thickness of 6mm and 10mm. The physical properties and chemical composition of this alloy is shown in Table **3**.

Table 3: Physical properties and Chemical composition of Base Plate

Material Identification	Composition	Classification (Aluminium Association)	Dimensions (LXBXH) mm	Number of Items
000884	AlMg4.5Mn/H111	AA5083-H111	500X400X6	1
000587	AlMg4.5Mn/H111	AA5083-H111	500X400X6	1

4 IMPLEMENTATION OF HAM PROCESS

This HAM process combines FSP and robotic MIG welding. First, metallic beads are welded on a substrate by a robotic MIG welding machine and then the concave profile of the overlapping beads are flattened by FSP to form a layer. New layers are repeatedly built on top of previous layer by sequentially fabricating beads with robotic MIG machine and FSP of the bead profiles as shown in Figure **20** [a, b].

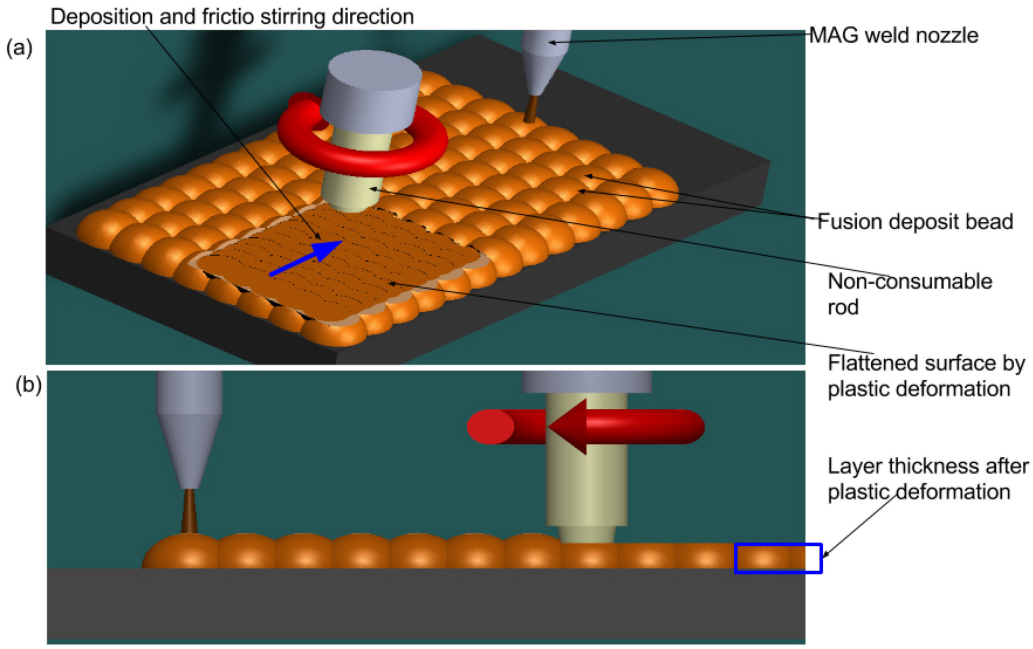

Figure 20: Robotic MAG and friction stirring process

This is a combined fusion-based and work-hardening AM process. It has been proven to improve immensely the mechanical properties of the built part in comparison to the base material [48] [49].

4.1 Designing Samples

Design simple 3D shapes (samples) of the final product. Each sample has been designed in the form of a plate with the following dimensions as shown in Table **4**.

Table 4: Design Samples Dimensions

	Layer Length (mm)	Layer Width (mm)	Number of Layers	Height (mm)
Sample 1 (HAM)	350	115	3	9
Sample 2 (MIG AM)	400	130	3	9

Length: The length is the amount of weld beads deposited on the substrate along the x-axis from the start to the end position during a single pass.
Width: This is the number of weld bead passes carried out during the building of a complete layer. It has been measured along the y-axis.
Height: This is the vertical radius of a weld bead as shown in Figure **21**.

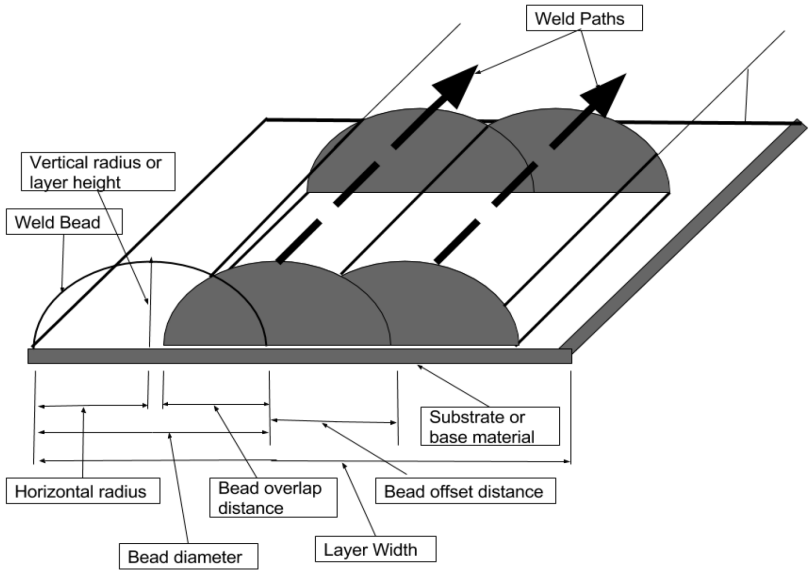

Figure 21: Weld Bead Geometry

4.2 MIG welding procedure

4.2.1 Setting Weld Deposition Parameters

Weld deposition parameters were established based on preliminary test on different weld samples. The best welding parameters from previous tests were used for this experimental procedure as shown in Table **5**.

Table 5: Weld beads deposition parameters

Deposition parameters for MIG AM process	**1 LAYER**
Current Density, A/mm	4
Wire feed, m/mm	10
Voltage, V	19.4
Current, A	169
Touch Handle Travel Speed, cm/min	50
Bead Overlap Distance along y-axis, mm	4
Bead Height, mm	3
Bead Diameter, mm	10
Layer Height, mm	3

4.2.2 Developing the MIG welding paths parameters

The weld beads are deposited and fabricated on the substrate along predefined paths, which were computed using equation (1)-(3).

For an n-number of weld paths,

$$y = D_1 + D_{0y}(n-1) \quad (1)$$

$$n = \frac{y - D_1}{D_{0y}} - 1 \quad (2)$$

$$D_{0y} = D_{cy} - D_{py} \quad (3)$$

$Where$:

$n = number\ of\ weld\ paths\ along\ y - axis.$

$y =\ Layer\ Width$

$D_1 =\ bead\ diameter$

$D_{0y} =\ bead\ offset\ distance\ along\ y - axis$

$D_{cy} = Current\ bead\ distance\ along\ y - axis$

$D_{py} = Previous\ bead\ distance\ along\ y - axis$

The number of weld paths or passes depends on the width of the sample.

From equation (1)-(3), and Table **5,** the number of weld paths can be computed.

Given:

$$y = 130mm, D_1 = 10mm, and\ D_{0y} = 6mm$$

$$130 = 10 + 6(n - 1)$$

$$n = \frac{130 - 10}{6} + 1$$

$$Number\ of\ weld\ paths\ or\ passes\ for\ each\ Sample\ = n = 21$$

To properly define/plan each weld path, individual weld passes has been described in detail:

a. First Weld Path or Pass:
    i. Define a reference position for weld touch, that is, x, y, and z, in reference to the robotic arm bed.
    ii. Define the weld start and end position; this is also known as the weld length.
    iii. Define the bead-offset distance; the distance between two positions along the y-axis or width.
    iv. Define the welding touch travel speed.
    v. Table **5** shows the used weld parameters.
b. Second Weld Path or Pass:
    i. Define the weld start and end position.
    ii. Define the bead-offset distance.
    iii. Define the welding touch travel speed.

iv. Table **5** shows the used weld parameters.

c. Repeat case (b) over a number of passes to generate the weld paths parameters required to build sample 1.

Table 6: Individual weld path parameters. The nth path is the last weld pass that makes up a complete layer width.

Deposition parameters for MIG AM process	Number of Weld Paths							
	1st	2nd	3rd	4th	5th	6th	7th	nth
Current Density, A/mm	4	4	4	4	4	4	4	4
Wire feed, m/mm	10	10	10	10	10	10	10	10
Voltage, V	19.4	19.4	19.4	19.4	19.4	19.4	19.4	19.4
Current, A	169	169	169	169	169	169	169	169
Weld Length, mm	400	400	400	400	400	400	400	400
Touch Handle Travel Speed, cm/min	50	50	50	50	50	50	50	50
Reference Position								
X reference position, mm	10	10	10	10	10	10	10	10
Y reference position, mm	10	16	22	28	34	40	46	130
Z reference position, mm	15	15	15	15	15	15	15	15
Bead Offset Distance along y-axis, mm	0	6	6	6	6	6	6	6
Bead Height, mm	3	3	3	3	3	3	3	3
Bead Diameter, mm	10	10	10	10	10	10	10	10
Layer Height, mm	9	9	9	9	9	9	9	9

4.2.3 Building Sample 1

Sample 1 is built by using parameters given in Table **6** , executing steps 1-8, and the robotic MIG welding equipment.

i. Step 1

   a. Cut a substrate in the form of a plate (Aluminium alloy AA5083) with dimensions large enough to embody each sample.

   b. Properly clamp the substrate to the robotic arm bed.

ii. Step 2

   Turn on the robotic arm and welding equipment.

iii. Step 3

a. Set robotic arm parameters from its control panel.
b. Set welding parameters from the welding equipment control panel.

iv. Step 4

Welding individual pass:

First pass:

a. Refer to Table **6** for input parameters.
b. Move weld touch to x and y reference position.
c. Set start position.
d. Set weld length.
e. Set travel speed.
f. Start welding; press button to start robotic arm movement.
g. Wait 5 ms and press trigger for weld touch to start weld bead deposition.
h. Press trigger to stop weld bead deposition at the end position.

v. Step 5

Second pass:

Add weld bead offset distance and repeat step 4 in order to build the second pass.

vi. Step 6

a. Repeat step 5 for the other passes or path until a complete layer is built.
b. Adjust z-reference by adding bead height (3 mm) to previous z-reference value (15 mm).

vii. Step 7

Repeat step 4 – 6 in order to build two additional layers; with each layer stacked on one another.

viii. Step 8

a. Wait for sample to cool down to room temperature.
b. Remove sample from clamp.
c. The resulting sample is shown in Figure **22**.

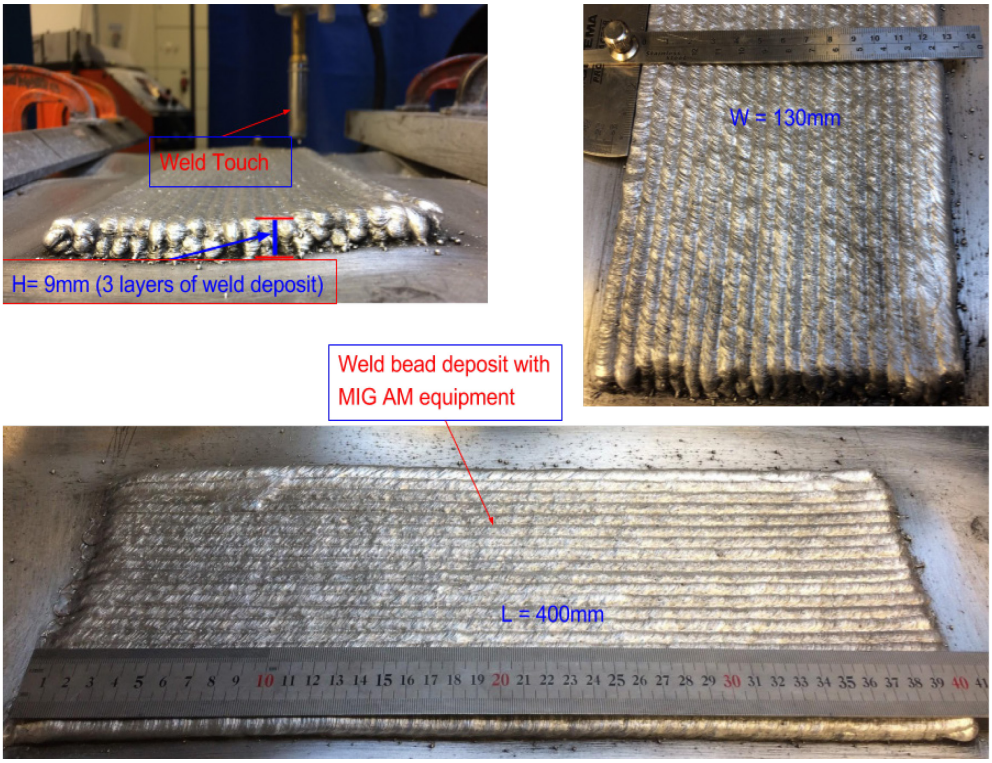

Figure 22: Sample 1 Weld Deposit

4.2.4 Building Sample 2

The building of sample 2 with MIG welding is similar to that of sample 1. Thus, in order to build Sample 2, refer to steps 1-8. The resulting built is shown in Figure **23**.

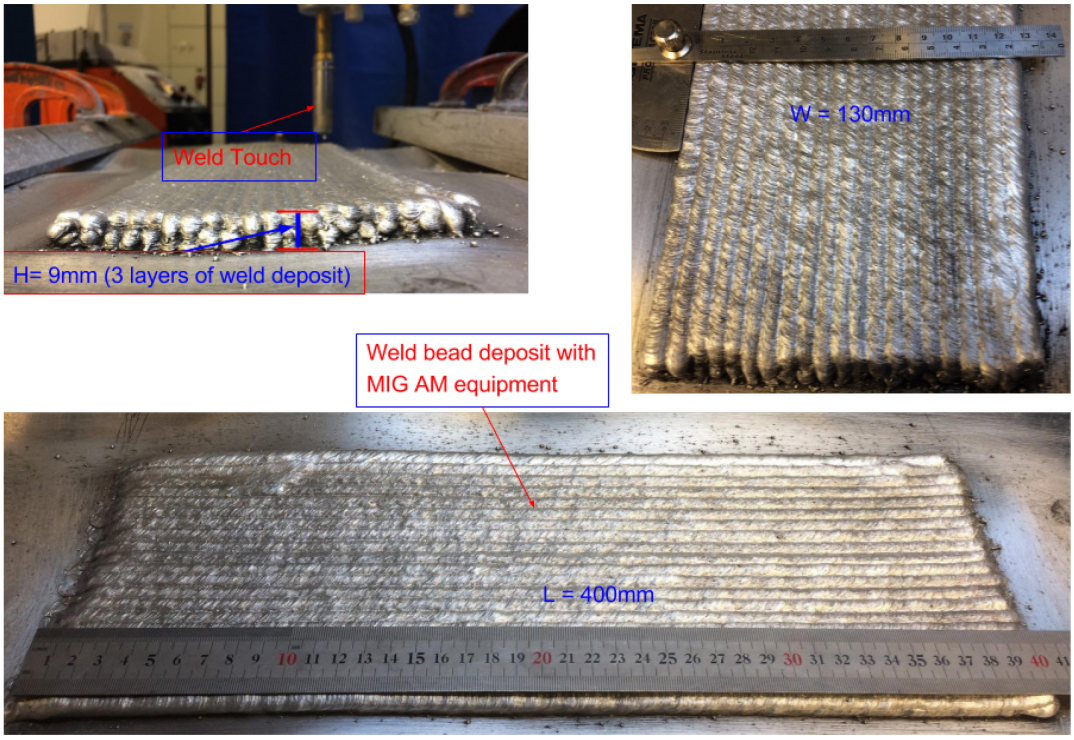

Figure 23: Sample 2 Weld Deposit

4.3 Friction stir processing procedure

The following steps was implemented for the FSP of the previously MIG welded sample.

4.3.1 Developing the FSP paths parameters

The weld path is the path along which the deposited beads are processed with the FSP tool. It should be noted that the processing paths are longitudinal to the weld deposition path.

a. Generating First Processing (weld) Path:
    i. Define weld length.
    ii. Define the weld start (reference) position.
    iii. Define the weld control method; that is, force controlled.
    iv. Define the penetration setting.
    v. Define the weld speed and tool rotation.

vi. Define the acceleration settings.

b. Generating Second Processing Path:
   i. Define weld length.
   ii. Define the weld speed and tool rotation.
   iii. Define the weld start position
   iv. Define probe-offset distance.
   v. Define the weld control method; that is, force controlled.
   vi. Define the penetration setting.
   vii. Define the acceleration settings.

c. Repeat case (b) over a number of times to generate the weld paths parameters required to process sample 1.

Table **7** shows the defined parameters for FSP of sample 1. It should be noted that the FSP condition was established based on a relationship between the tool travel speed and rotation. An intermediate condition has been applied [11]

That is,

[11]
$$2 \geq \frac{rotation, \Omega\ (rpm)}{travel\ speed, v\ \left(\frac{mm}{min}\right)} \leq 4 \qquad (4)$$

For this experiment, $\Omega = 450rpm\ and\ v = 150mm/\min\ was\ used.$

Table 7: FSP Parameters

FSW Processing Parameters	Number of Weld Paths					
	1st	2nd	3rd	4th	5th	nth
Weld Length, mm	360	360	360	360	360	360
Speed and Rotation Settings						
Tool Rotation, rpm	450	450	450	450	450	800
Weld Speed, mm/min	150	150	150	150	150	150
Reference Position						
X start (reference) position, mm	850	850	850	850	850	850
Y start (reference) position, mm	235	229	223	217	211	169
Probe Offset Distance along y-axis, mm	0	6	6	6	6	6
Penetration Settings						
Start penetration position, mm	9.2	9.2	9.2	9.2	9.2	9.2
Weld position, mm	0.2	0.2	0.2	0.2	0.2	0.2
Tool plunge speed, mm/s	0.15	0.15	0.15	0.15	0.15	0.15
Weld force reference, kN	18.5	18.5	18.5	18.5	18.5	18.5
Dwell Settings						
Dwell time, s	4	4	4	4	4	4
Acceleration Settings						
Time	0.5	0.5	0.5	0.5	0.5	0.5
Deceleration	0.5	0.5	0.5	0.5	0.5	0.5

4.3.2 FSP of Sample 1

The following steps have been adopted in processing sample 1. Sample 1 was built from an additive manufacturing process of MIG weld deposition by implementing steps 1-5.

i. Step 1
   a) Clamp sample 1 to the FSW machine bed.
   b) Turn on FSW machine.

ii. Step 2
   a) Manually assemble tool and set probe pin length to extend 9mm from the concave shoulder.
   b) Clamp tool to a sleeve.
   c) Clamp the corresponding assembly to the FSW machine spindle.
   d) Tilt spindle head by 2^0.
   e) Check for leakages around the tool by turning on the water coolant from the parameter menu of the FSW machine control panel.

iii. Step 3

Setting Processing Parameters for first weld path:

a) Refer to Table **7** for processing parameters.
b) Set processing parameters from the control panel.
c) Review input parameters.
d) Press start to begin the friction stir processing. At the end position, the tool retracts out of the sample and stops rotating.

iv. Step 4

Setting Processing Parameters for Second weld path:

a. Refer to Table **7** for processing parameters.
b. Set probe-offset distance.
c. Set processing parameters from the control panel.
d. Review input parameters.
e. Press start to begin the friction stir processing. At the end position, the tool retracts out of the sample and stops rotating.

v. Step 5

a. Repeat step 4 until the whole weld beads on sample 1 are fully processed.
b. Allow sample to cool down to room temperature before unclamping it from the bed.

The resulting processed workpiece is shown in Figure **24**.

It should be noted that all variables for both weld deposition and FSP have been kept constant during this experimental work in order to simplify the development process. Thus, the optimum value for each variable are yet to be identified. Future work should thus look into parameter optimization by varying some of the constant variables.

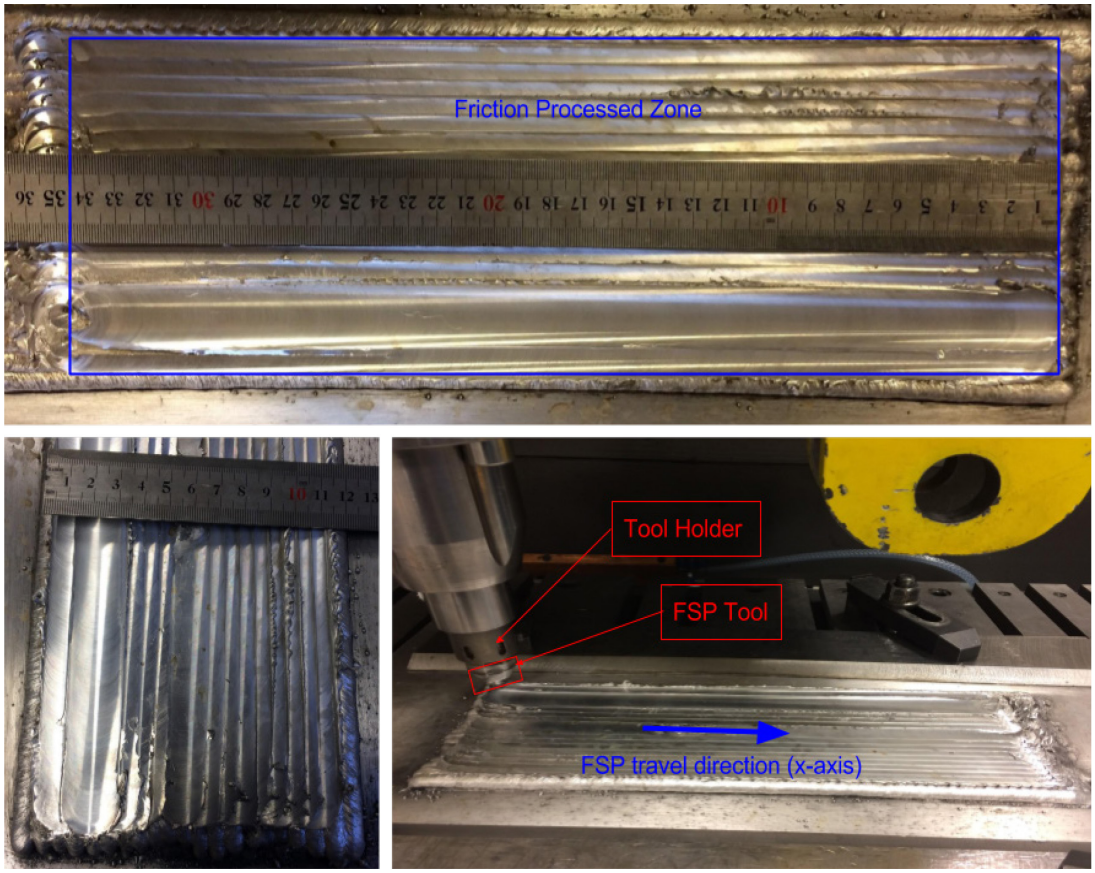

Figure 24: FSP of Sample 1

4.4 Probe Failure

There lies a relationship between the stresses generated on FSP tool (specifically on the probe pin) and the number of weld bead layer being processed. Figure **26** shows the forces and torque produced during the FSP of 3-layer weld deposit. It was observed that the normal forces (F_z) and lateral forces (F_x) were relatively the same, but axial force F_y, Torque (T), and processing temperature increased considerably as the number of processed layer changed. This gave rise to high stresses at regions between the probe and shoulder. As such, repeated probe fracture was observed while carrying out multi-pass processing of 3-layers at various point. Figure **25** shows the number of fractured probes during the processing of various 3-layers samples.

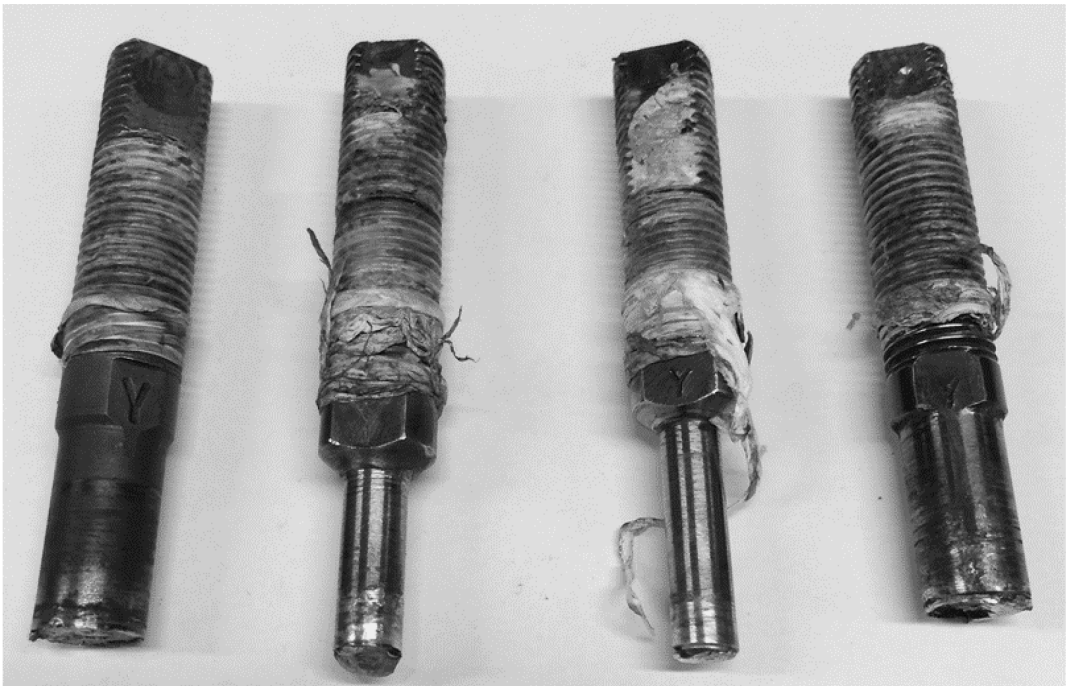

Figure 25: Fractured Probes

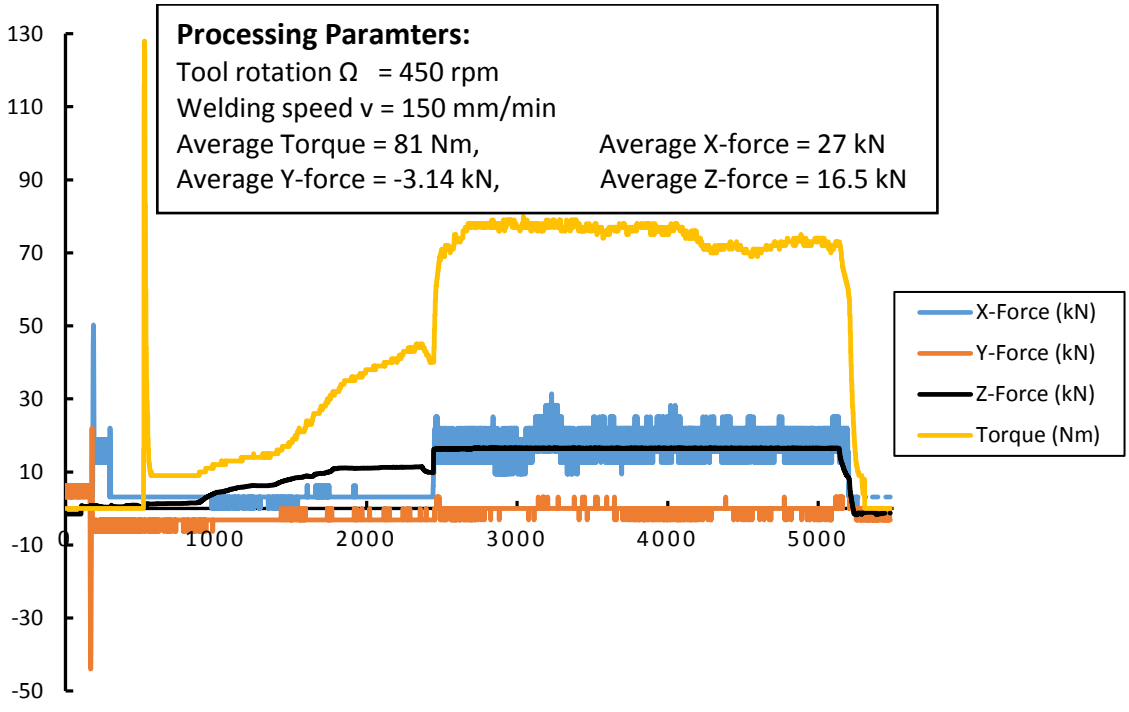

Figure 26: Generated Forces from FSP

An analysis of static stresses during FSP shows that,

$$Normal\ stress, \sigma_n = \frac{Fz}{A} \quad (5)$$

$$Shear\ stress, \tau = T_s/J_p \quad (6)$$

$$Bending\ stress, \sigma_b = M * z/I \quad (7)$$

$$Mx = Fx * L/2 \quad (8)$$

$$My = Fy * L/2 \quad (9)$$

$Where: Fz = tool\ vertical\ force, T_s = spindle\ torque,$
$A = crosssectional\ area\ of\ probe\ pin, and$
$J_p = polar\ moment\ of\ area, M = bending\ moment,$
$z = vertical\ distance\ away\ from\ neutral\ axis,$
$I = moment\ of\ inertia\ around\ the\ neutral\ axis,$
$Fx = Lateral\ or\ travel\ force, \quad Fy = force\ along\ the\ y - axis.$

Another reason for subsequent fracture of probe during processing of 3-layer bead deposit can be explained using Equation (5) and (6). From equation (5), it can be deduced that as the F_z increases, the stress around the also increases at relatively high temperature. In addition, it can be seen from equation (6) that, as the torque increases, the shear stresses are bound to increase. The resultant increase in stresses while processing 3-layers simultaneously at high temperature could also have led to the probe fracture at different locations on the workpiece.

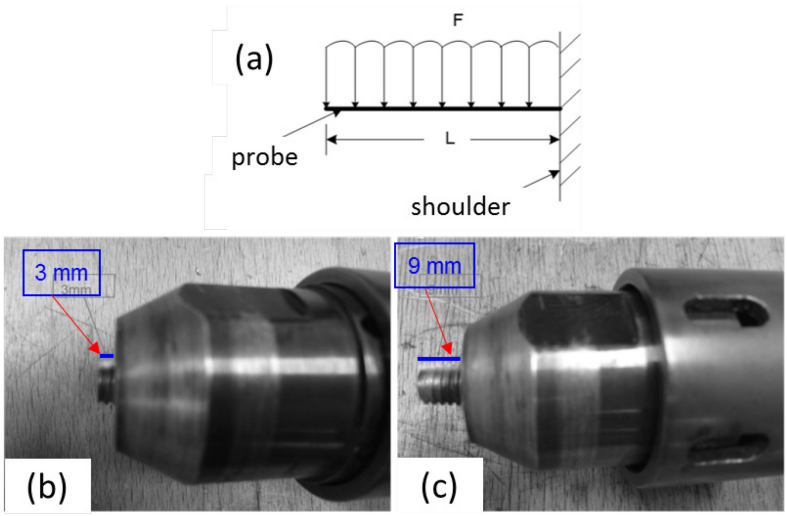

Figure 27: Processing region of probe

Figure **27** shows the length of probe extending from the tool shoulder when carrying out FSP on 1-layer and 3-layers. The bending stress produced between the probe and the shoulder is synonymous to that experienced on a cantilever with distributed load as shown in Figure **27**a. Figure **27** (b) and (c) show the tool with extended pin length L of 3 mm and 9 mm respectively. Using Equation (7)-(9) with the probe parameters, it shows that the bending moment and the bending stress is higher for the probe in Figure **27**c than that in Figure **27**b, even though the lateral forces in both use case were relatively the same during experimentation. The result of the above expression could also be the reason for fracture of the probe in Figure **25** when it was used to process 3-layers of weld bead simultaneously.

Rajiv et al. [12] attributed probe fracture to the temperature gradient from the root of probe to the tip of the probe, thereby leading to variation in workpiece strength around the friction stirred zone. As such, the workpiece strength is highest at the bottom of the probe and as the tool rotates the forces within the advancing and retreating side changes, thereby producing cyclic loading similar to a rotating beam bending fatigue specimen. This could eventually lead to probe failure in due time. It was also observed that no probe failed/fractured during the processing of one layer. This can be attributed to the fact that the forces and torque generated during the processing produced stresses lower than the fracture strength, even at the high temperatures.

5 TESTING PROCEDURE

The previous chapter described the HAM implementation (experimental procedure). This chapter describes the test approach for a number of specimens. Section 5.1 describes the extraction process of the various test specimen. The tensile, bending, and hardness testing, are described in Section 5.3, 5.4, and 5.5 respectively.

5.1 Specimen extraction plan

Figure **28** shows a 3D model of sample 2 with similar dimensions as the produced sample. It also shows the positions where the test specimens were extracted. This model served as a guide for extracting the specimens from the sample. Test in both longitudinal and transversal directions were carried out on the specimens to observed discrepancies on test data.

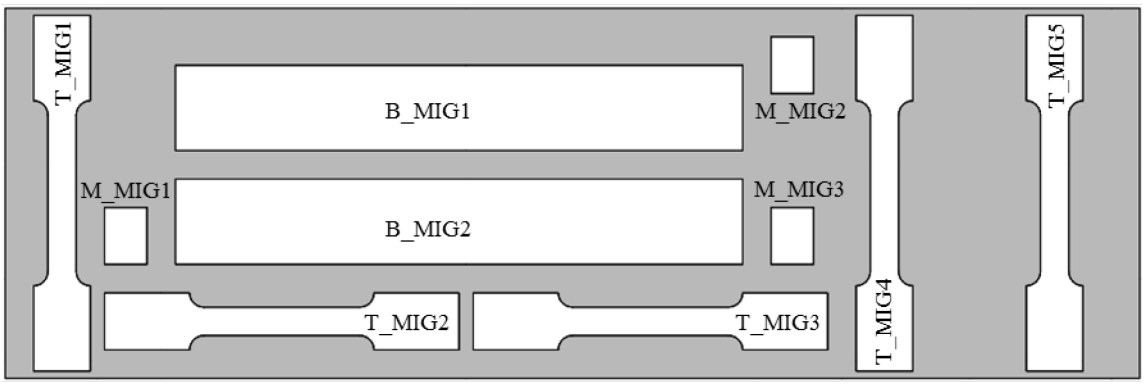

Figure 28: Specimen Extraction Model for Sample 2

Where:
T = Tensile test, B = Bending test, and M = Microstructural test.

Similarly, a number of specimens were extracted from Sample 1 as depicted in a 3D model shown in Figure **29**. The model is of length 350mm and width 115mm, which is equivalent to the FSP zone of sample 1.

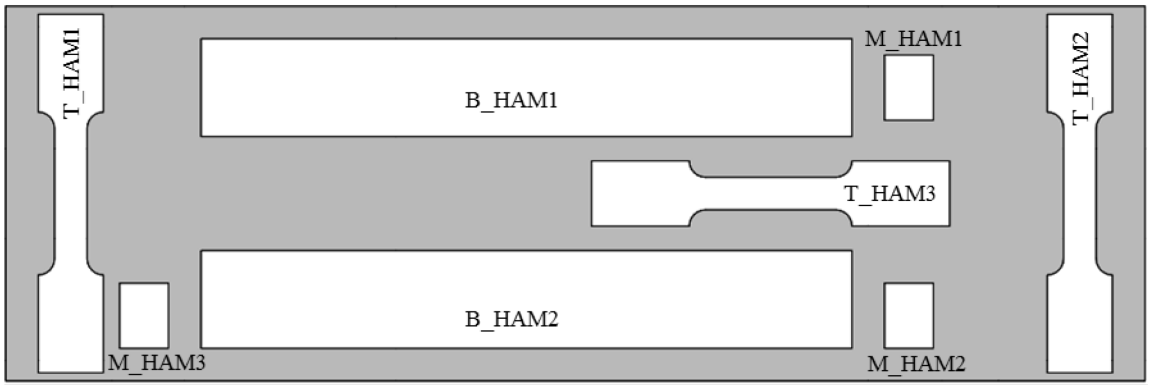

Figure 29: Specimen Extraction Model for Sample 1

5.2 Optical macroscopic and microscopic testing

In order to understand the macrostructural and microstructural evolution of the samples, several specimens were extracted and observed under optical microscope.

The specimens were sufficiently grind with 15 µm and 20 µm grain size grit to removed rough surfaces and scratches. They were further polished with 3 µm and 1 µm grain size grit, with a diamond fluid to enhance the polishing. The grinding and polishing were carried out on Struers LaboPol-2 and Struers LaboPol-5 machines respectively. At random times, ethanol was used to clean the specimens after grinding and during polishing.

The specimens for optical microscopic observation were etched with hydrofluoric acid (HF) just after polishing and rinsing with ethanol, to reveal the macrostructure and microstructure. The resulting specimens are shown in Figure **31**. The macrostructure and microstructure of the resulting specimens were observed under Wild Macroscope M420 (Figure **30**a) and Nikon Epiphot 200 microscope (Figure **30**b) respectively with Nikon Digital Sight DS-UI.

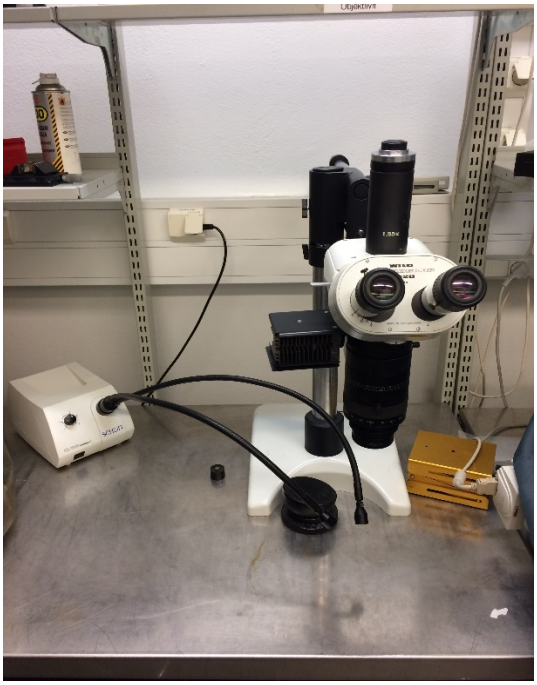

(a) Optical macroscope

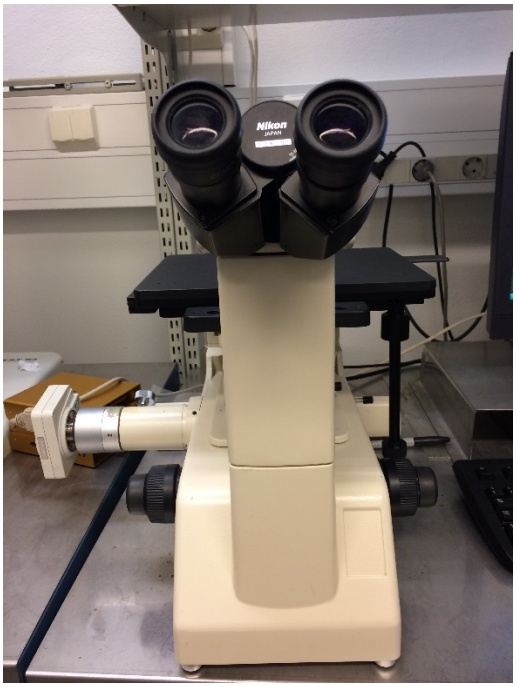

(b) Optical microscope

Figure 30: Equipment setup for Optical macrostructural and microstructural observation

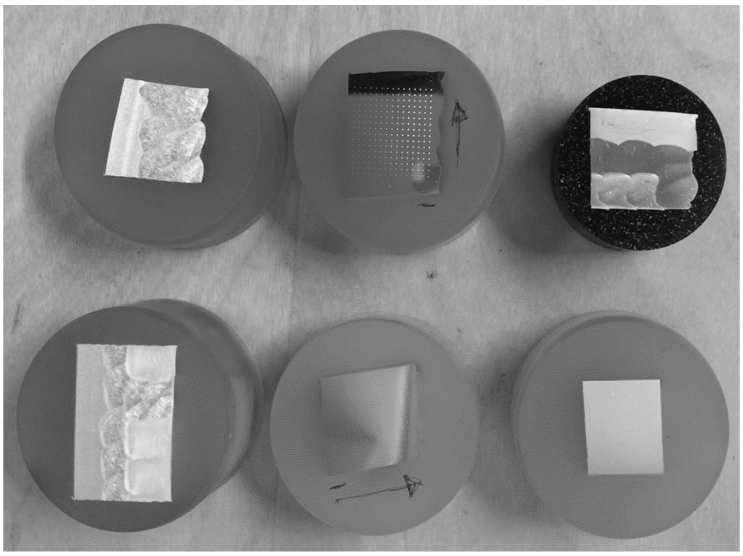

Figure 31: Specimens from As-MIG-welded and HAM samples for Metallurgy Analysis

5.3 Microindentation hardness testing

This is a technique commonly used to study fine scale changes in hardness. In this work, the hardness test is used to determine the surface hardness of MIG-welded specimen and HAM specimen. In addition, the test was intentionally used to check the homogeneity of the grains across different multi-pass locations.

Two specimens were extracted for the hardness test; one specimen from sample 1 and the other from sample 2. The specimens were also fine-ground and polished using the Struers LaboPol-2 and Struers LaboPol-5 machine respectively, and applying similar grainsize grit as with the optical microscopy specimens but were not etched.

The micro-indentation hardness measurements were carried out on a CMS instrument. Table **8** presents the indentation parameters and the applied indenter properties.

Table 8: Microindentation hardness input parameters

Indentation Parameters
Acquisition rate: 10.0 Hz
Max Load: 5000 mN
Loading rate: 10000 mN/min
Unloading rate: 10000 mN/mm
Pause: 10s
Indenter Properties
Type: Vicker
Serial Number: VH-81
Material: Diamond

Linear patterned hardness profiles were created for each specimen by defining the width and height of the indentation matrix (16 X 15), the spacing of dents (1 mm), starting point, and offset distance (1 mm) from the edges of the specimen as shown in Figure **32**.

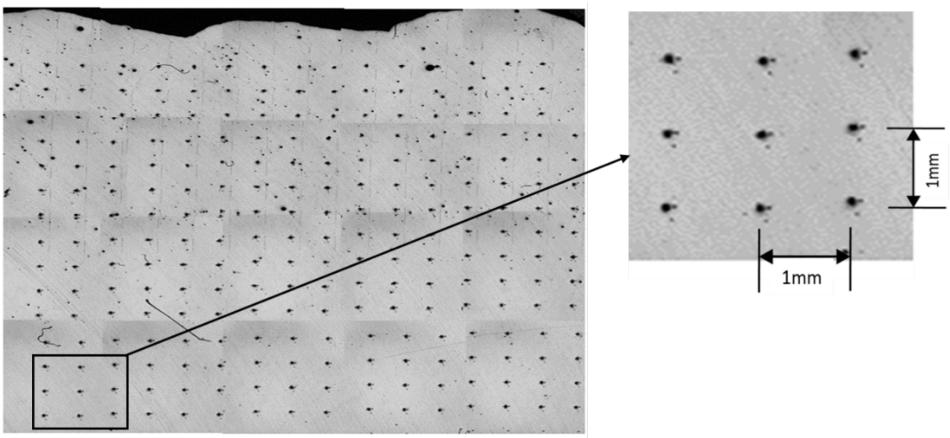

Figure 32: Linear patterned hardness profile

5.4 Tensile testing

An MTS 858 servo-hydraulic universal equipment was used for the tensile testing. It comprises a load cell of $\pm 25\ kN$ and an extensometer with a range of 0-25%. The speed of test was 1 mm/mins and 2 mm/mins in the elastic and plastic region respectively throughout the test specimens. The tensile testing was carried out based on SFS-EN ISO 6892-1 standard. Figure **33**(a) and (b) shows the various tensile test specimens extracted from sample 1 and 2. The mechanical properties of the samples were computed from the test data by applying Hooke's and Ludwik laws, and static equations.

Hooke's Law:

$$\sigma = K\varepsilon \tag{10}$$

$$Nominal\ Stress, S = F/A_0 \tag{11}$$

$$Nominal\ Strain, e = \frac{l - l_0}{l_0} \tag{12}$$

$$True\ Stress, \sigma = \left(\frac{F}{A_0}\right) = S(e + 1) \tag{13}$$

$$True\ Strain, \varepsilon = \ln(e + 1) \tag{14}$$

Ludwik Law:

$$\sigma = Ke^n \tag{15}$$

$$Tensile\ Toughness, U_T = \frac{Energy}{volume} = \int_{\varepsilon_0}^{\varepsilon_f} \sigma d\varepsilon \quad (16)$$

$$Bending\ Toughness, U_B = Energy = \int_{e_0}^{e_f} F de \quad (17)$$

Thus, equations (10)-(17) have been applied to test data in computing the nominal stresses and strains, true stresses and strains, young modulus, yield strength, and toughness/energy.

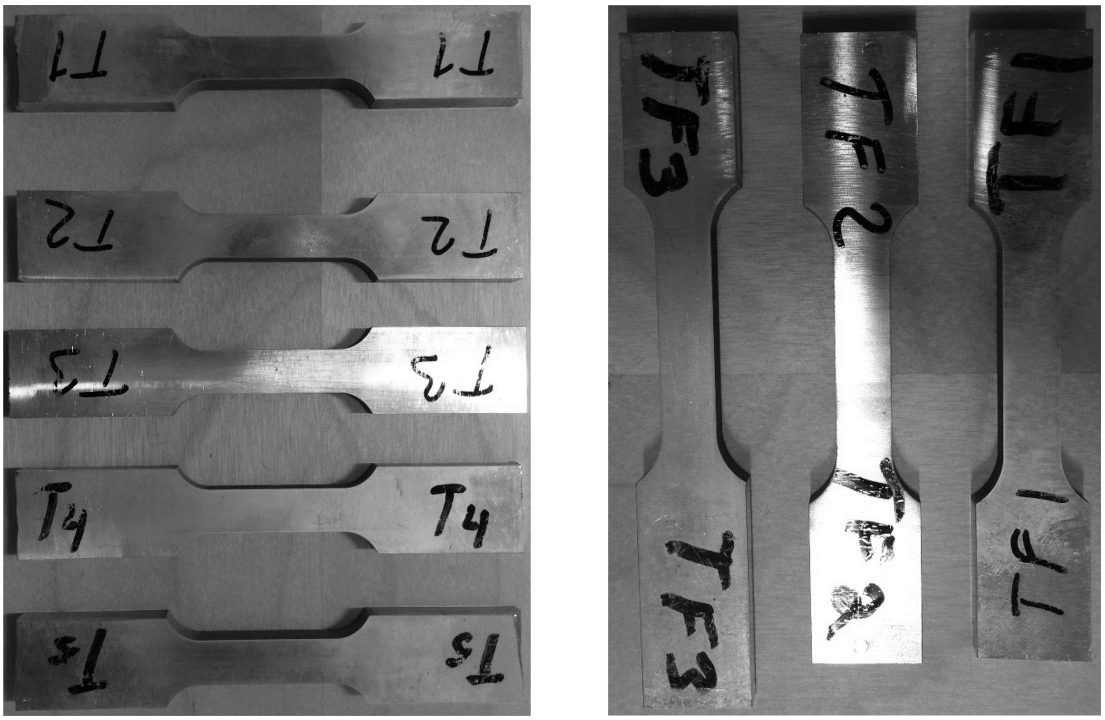

(a) Sample 2 (As-MIG-welded) (b) Sample 1 (HAM sample)

Figure 33: Tensile Test Specimens

5.5 Bending testing

The bending tests were carried out on an MTS 810 material test equipment using a 3-point bending test setup. It comprises a servo hydraulic plunger with a 100 kN force capacity and sets of rollers. The plunger is equipped with a 12 mm diameter roller while the bed or support is equipped with two supporting rollers of 50 mm in diameter. The test was setup to allow

for 50 mm spacing between the supporting rollers. A displacement rate of 20 mm/mins was applied to all specimens during the bending test. Figure **34**(a) and (b) shows the various bending test specimens extracted from sample 1 and 2.

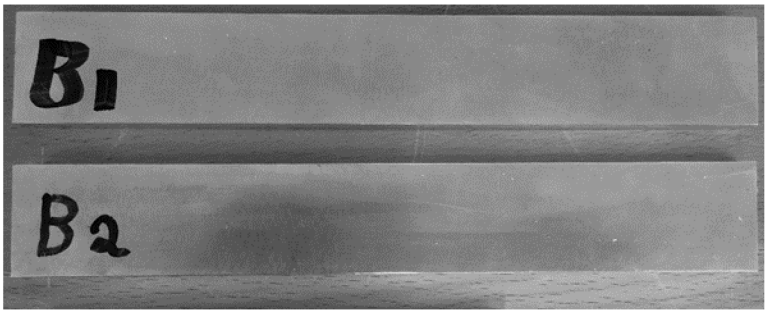

(a) Sample 2 (As-MIG-welded)

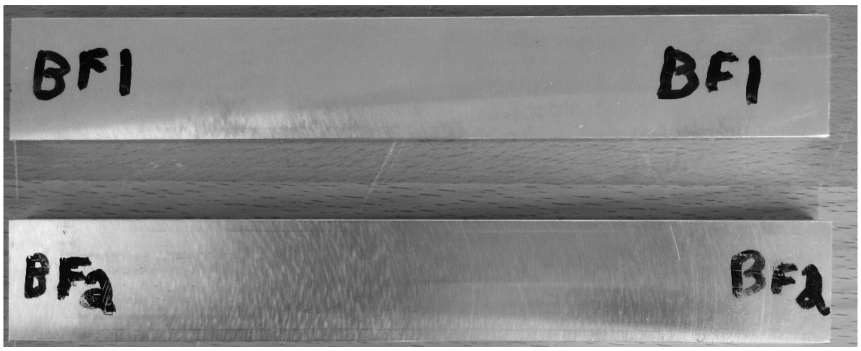

(b) Sample 1 (FSP zone sample)

Figure 34: Bending Test Specimens

Some of the extracted specimens were observed under tensile and bending test while metallurgical analysis were carried out on the other specimens. The results of the test specimens and their interpretation are presented and discussed in the next chapter.

6 RESULTS AND DISCUSSION

The previous chapter described the test approach and data acquisition. This chapter provides an elaborate discussion on the result of the test, as well as compares the results with other AM processes. It also presents a comparison in terms of quality between the MIG-welded sample (sample 2) and HAM sample.

Recall that, the key objective (requirement) of developing this process was to increase the strength (quality or performance index) of arc-based additive manufactured metallic parts. Thus, the objective function of components manufactured by this process is to:

$$Objective\ function = Maximize \begin{cases} Ultimate\ tensile\ strength, \\ Yield\ strength, \\ Ductility\ or\ elongation, \\ and\ Fatigue\ strength. \end{cases}$$

6.1 Metallurgical analysis

Micro-casted (weld bead deposited) parts exhibit numerous microstructural defects that limits their performance in terms of mechanical properties. These defects are similar to those experienced in traditional metal casting [39].

6.1.1 Macrostructure Analysis

Figure **35** and Figure **36** show the optical macrograph of As-MIG-welded (sample 2) and FSP zone (sample 1) respectively at different positions around the samples. In Figure **35**(a) and (b), numerous pore holes (voids) are observed both in transversal and longitudinal directions of sample 1. Several past research have noticed micro voids from weld deposition and have proposed various ways to reduce the amount of voids from welding by properly adjusting the deposition parameters. However, most of these solutions do not fully eliminated

the voids. By combining FSP with MIG welding, the final sample becomes free of voids as shown in Figure **36**(a) and (b).

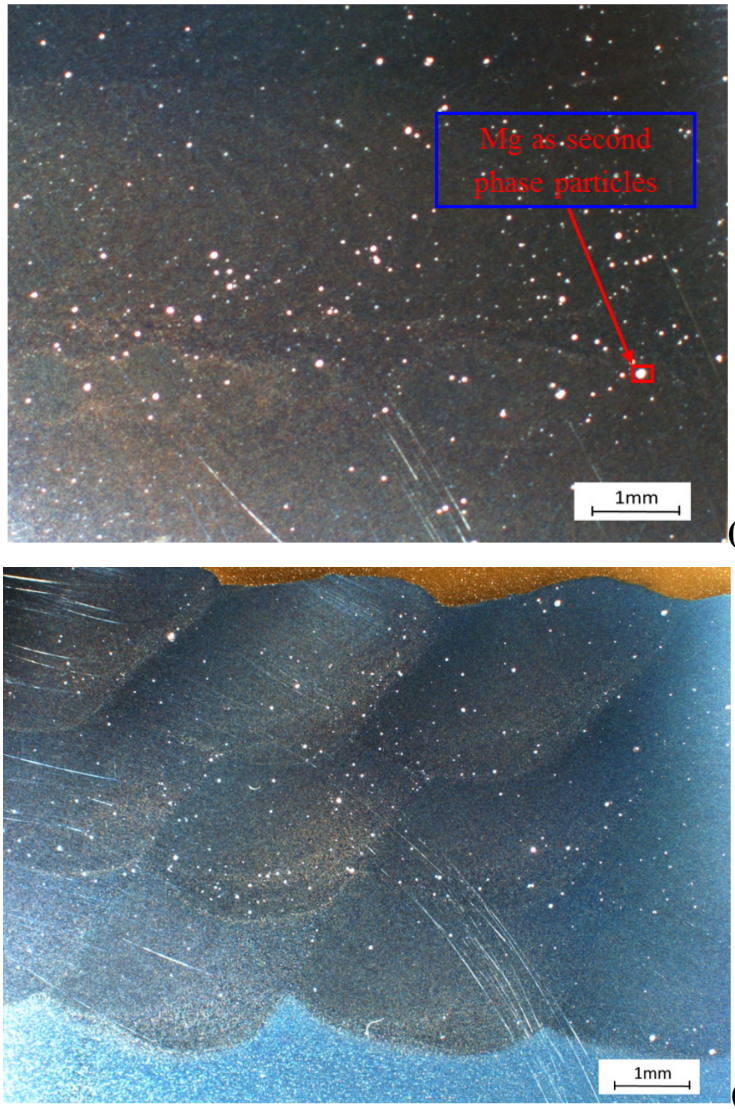

Figure 35: Optical Macrograph of As-MIG-welded workpiece (sample 2)

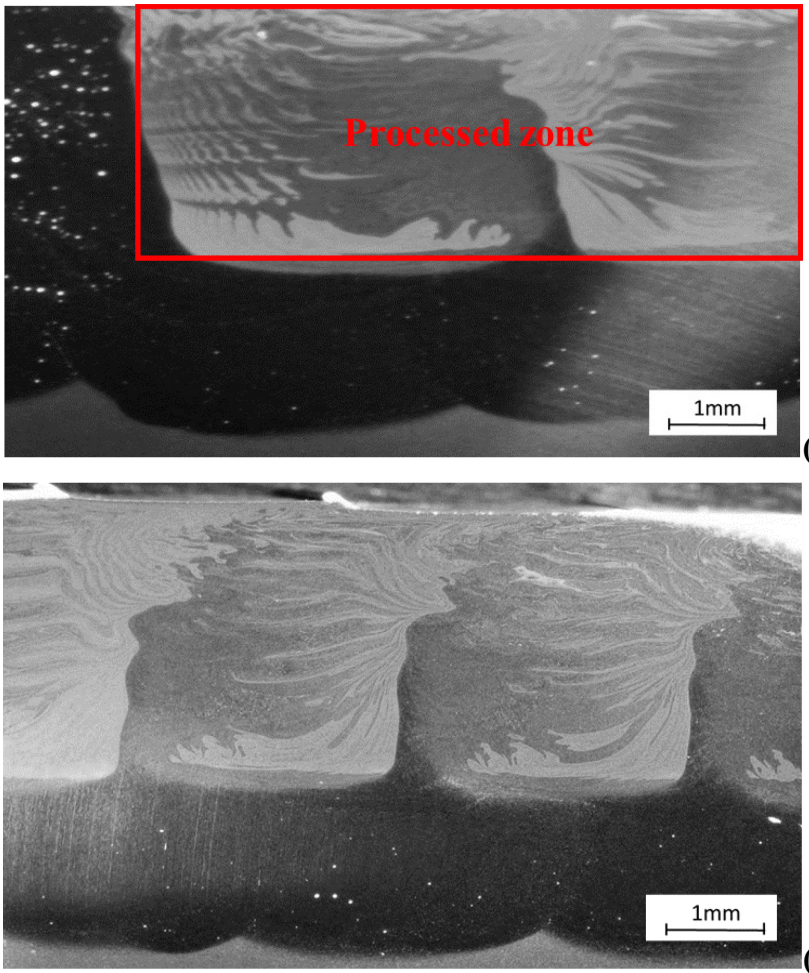

Figure 36: Optical Macrograph of FSP workpiece (sample 1)

6.1.2 Microstructural Analysis

Figure **37** and Figure **38** shows the optical microstructure of sample 1 and 2 respectively. It can be clearly observed that the grains have been refined and uniformly distributed in Figure **38** compared to Figure **37**. Numerous smaller grains, and reduced grain spacing and boundaries can also be observed in Figure **38** in comparison to Figure **37**, which can be attributed to material flow (grain compaction) or plastic deformation that occurred around the stirred zone. Furthermore, second phase particles (black color) can also be observed in the microstructures of Figure **37** and Figure **38**.

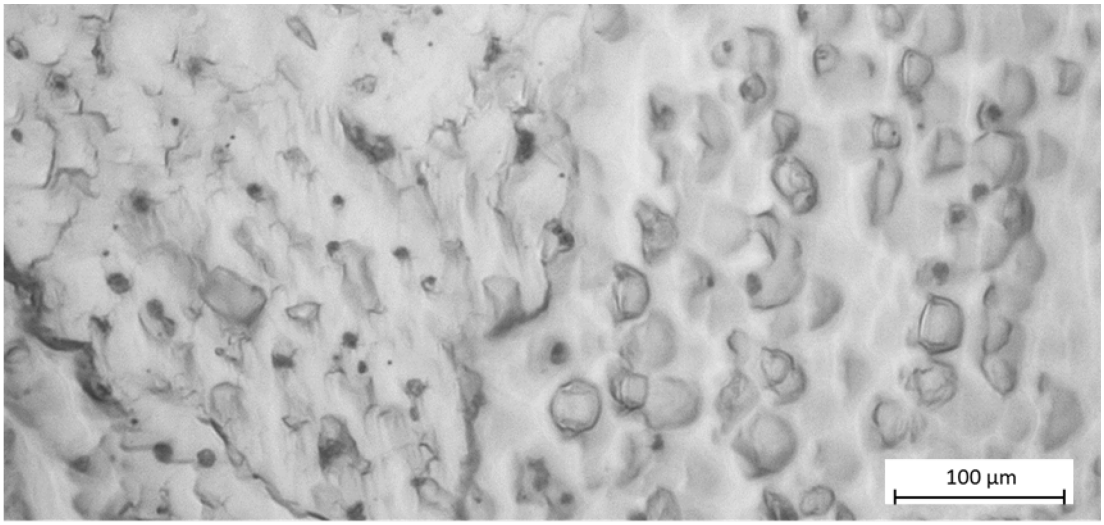

Figure 37: Optical micrograph of specimens extracted at specific position of sample 2

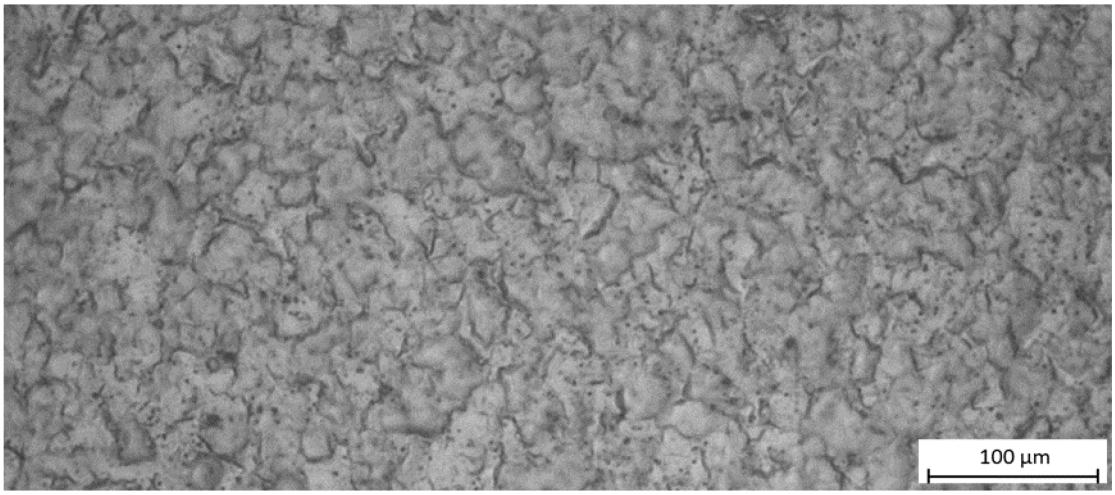

Figure 38: Optical micrograph of specimens extracted at specific position of sample 1

A more profound view of the microstructures reveal that the particles are predominantly Magnesium precipitates, as shown in Figure **39**. However, the size of the particles and their spacing clearly differ in sample 1 and 2. In Figure **39**(a), the particles are larger in size and widely spaced, which could be attributed to the heat input, or cooling rate of the MIG welded sample (sample 2). Meanwhile, in Figure **39**(b), the numerous small size particles that are uniformly distributed can be observed due to plastic deformation during FSP.

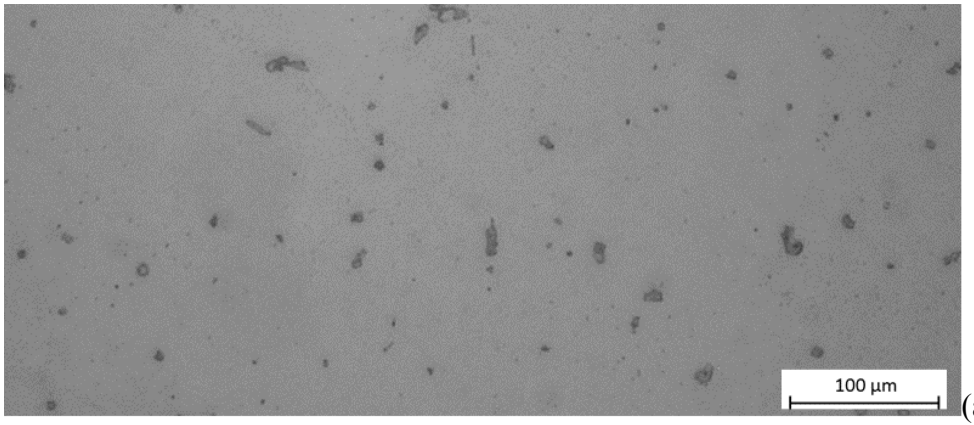

Figure 39: Particle distribution across specimens under Optical microscope. (a) Particle distribution in sample 2 (as-MIG-welded), (b) Particle distribution in sample 1 (HAM sample).

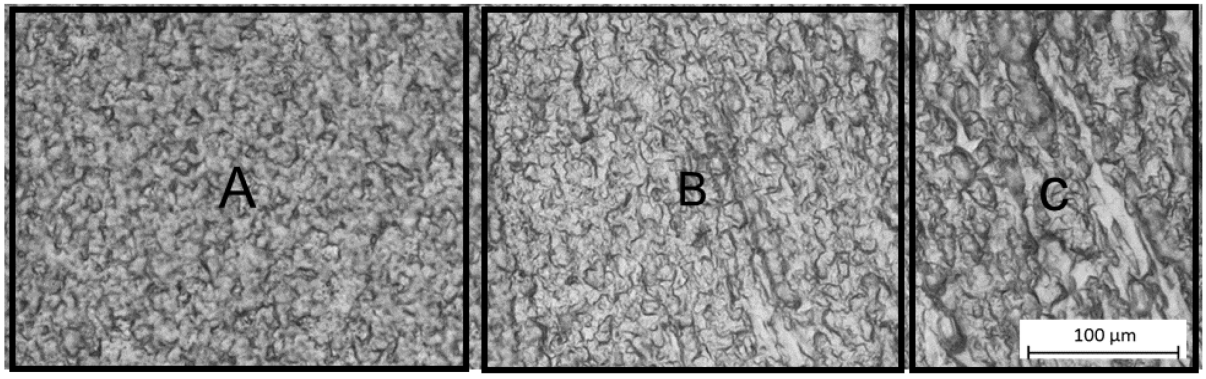

Figure 40: Boundary between FSP zone and MIG-welded zone under optical microscope

Variation in grain sizes and boundaries can also clearly be seen in Figure **40**. From the figure, the region which surrounds *A* is the SZ or TMAZ; as such, the grain sizes are smaller with numerous dislocations or grain boundaries. The region which surrounds *C* is the MIG-welded

zone; the grains are more coarsened and exhibit dendritic or elongated shape as a result of the cooling rate and heat input during the MIG welding process. *B* region, which is also known as HAZ during FSP, have grain sizes that are between those of *A* and *C*, and dendritic and columnar shape grains can evidently be seen in this region. The dendritic grains are mainly concentrated on the right side of *B*-region while the columnar grains are concentrated on the left side of *B*-region, because of the direction of heat flow and normal forces moving from *A* to *C*.

Another profound observation was the elimination of voids from the As-MIG-welded sample after FSP as can be seen in Figure **36**. These voids usually acts as regions for cracks initiation. By eliminating these voids, the endurance limit of the sample increases, thereby improving the fatigue strength of the sample.

Jata et al. [50] observed equiaxed fine grains around the FSP zone of a rolled and annealed 1050 aluminium alloy. They also observed the effect of temperature on grain refinement. Fine grains were observed and grain sizes were less than 2 μm around FSP zone at temperature of 470k [50].

Yang et al. [31] observed coarsened columnar grains around the melt zone of a multi-pass MAG welding using 304 stainless steel filler wire. Because of these large grain sizes observed from the welding processes, they developed a micro-roller mechanism for continuous work hardening of the grains in order to reduce their sizes.

Sindo K. [51] observed a relationship between the heat input Q and the welding speed V, and concluded that the ratio of Q/V could be used to explain the microstructural evolution of weld beads along the fusion line and weld centerline. That is, the cooling rate decreases with increasing heat input to weld speed ratio Q/V, and thus the dendritic arm spacing or cell spacing should increase as the ratio increases, and this results in more coarsened grains [52].

6.2 Microindentation hardness behavior

Figure **41** shows a contour plot of the microindentation hardness for sample 2. The sample measured an average Vickers hardness value of 80.40HV, which is less than the 95HV hardness value for 5XXX series single-pass MIG-welded aluminium. This can be attributed to the undesirable heat treatment (heat cycle), nucleation, and excessive grain growth during multi-pass and mult-layer MIG welding, thereby leading to the softening of the resulting built sample. The specimen measured Vickers hardness value of 92HV maximum and 54HV minimum. The significantly low value of Vickers hardness at random position around the measured specimen could be attributed to the indenter creating dents on locations coincidental to micro-void positions. It was also observed that the hardness of the base plate (A5083 aluminium alloy) reduced drastically to mean value of 75HV owing to this same thermal cycle effect during the MIG welding process.

However, the HAM sample recorded an average Vickers hardness of 95 HV and a maximum value of 105 HV. This can again be attributed to the grain refinement, generation of new dislocations, and sufficient removal of micro-voids during plastic deformation. Figure **42** presents a contour plot of the hardness profile.

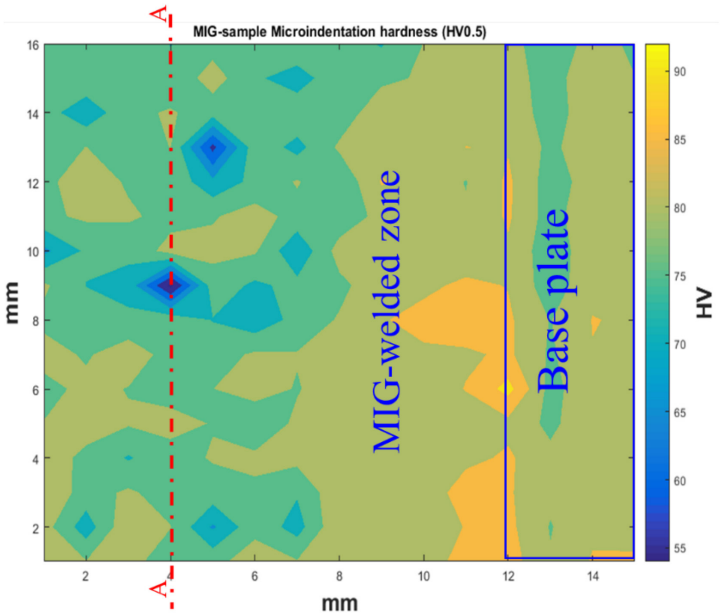

Figure 41: MIG-sample hardness contour plot

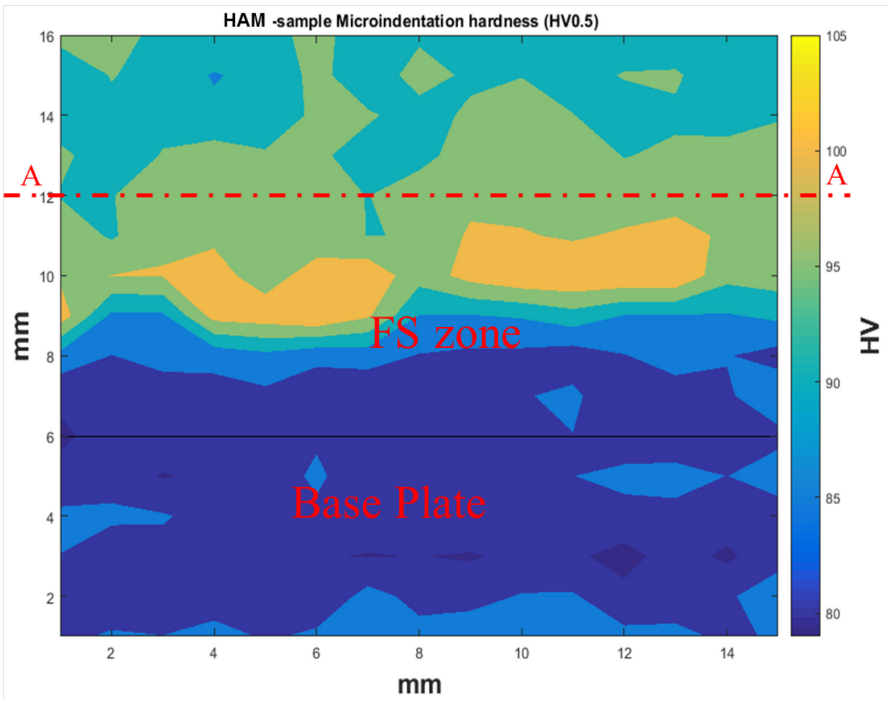

Figure 42: Contour plot of HAM sample

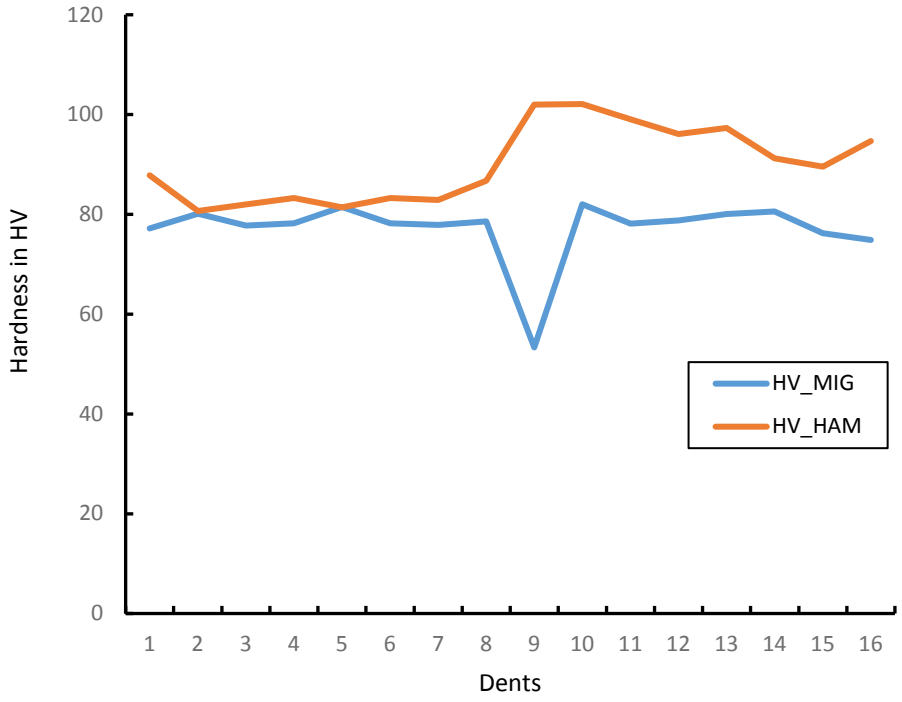

Figure 43: Linear plot of MIG and HAM Hardness specimen through section A-A

Figure **43** shows a linear plot that compares the hardness values of sample 1 and 2 passing through section A-A. Section A-A is located 4 mm below the top surface of the MIG AM and HAM specimens. It can be clearly observed from the plot that the hardness values of HAM sample at every indented location is significantly higher than those of the MIG AM sample.

6.3 Tensile behavior

Recall from Figure **28** and Figure **29** that, T_MIG1-T_MIG5 are the tensile test specimens extracted at different location of the As-MIG-welded sample (Sample 2 or base material) while T_HAM1-T_HAM3 are the tensile test specimens extracted from different positions of HAM sample (Sample 1). In Figure **44** and Figure **45**, it is obvious that Sample 1 and 2 behaved differently under tensile loading. T_MIG1-T_MIG5 had similar behavior in the elastic and plastic region. Their yield strength was 147 MPa each and percentage elongation was approximately 22% each, in both longitudinal and transverse direction. Meanwhile, T_HAM1 had yield strength of 167 MPa, and T_HAM2 and T_HAM3 had yield strength of around 194 MPa, with significant differences in their elongation. T_HAM1, T_HAM2, and T_HAM3, had percentage elongation of around 4%, 7.5%, and 30% respectively. T_HAM1 and T_HAM2 were extracted along the transversal direction of sample 2. Their considerably low elongation could be attributed to insufficient material flow along the transverse direction during multi-pass friction stir processing. It could also have been because of inadequate overlap distance between the processed paths (multi-pass) along the transversal direction; an overlap distance of 2mm on the root-side and 0.5mm on the tip-side of the truncated conical probe pin.

I propose that the overlap on the root and tip-side of the probe pin should be set larger during future work.

T_HAM3 showed considerable higher UTS and Toughness compared to other specimens. A summary of the variation in mechanical properties in regards to the various tensile tests specimen is shown in Table **9**. These results can be correlated with those observed by Mishra et al. [39] on AA5083 Al alloy after FSAM. The overall mechanical properties improved due

to grain refinement and grain size reduction. Borrego et al. [53] observed different behavior in the mechanical properties but similar microstructural behavior of AA5083 Al alloy after FSP in comparison to the results of this thesis work. They observed that the UTS and elongation of the FSP specimen were slightly lower than those of the base material [45].

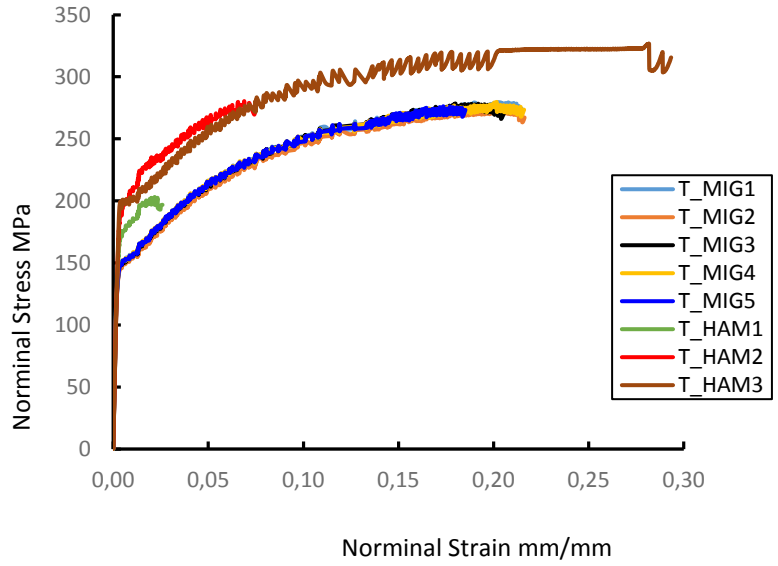

Figure 44: Nominal Stress-Strain of Sample 1 and 2

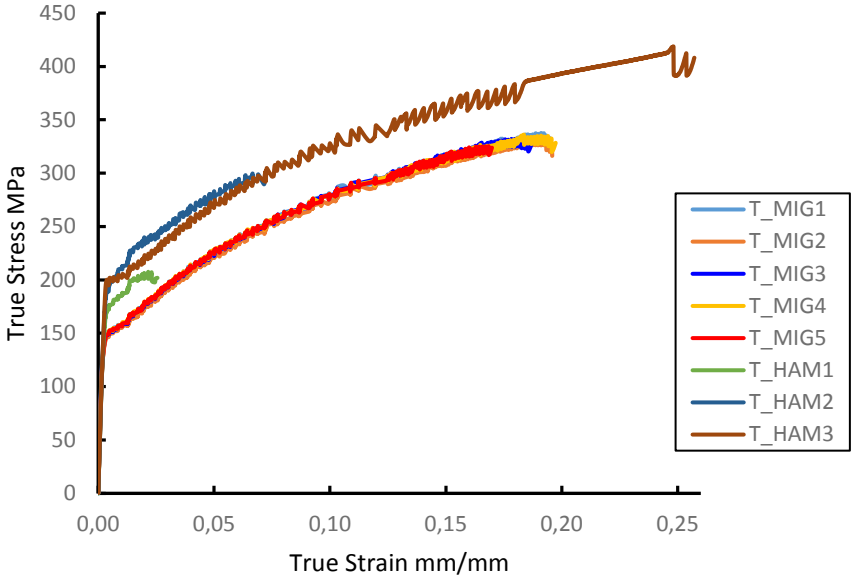

Figure 45: True Stress-Strain of Sample 1 and 2

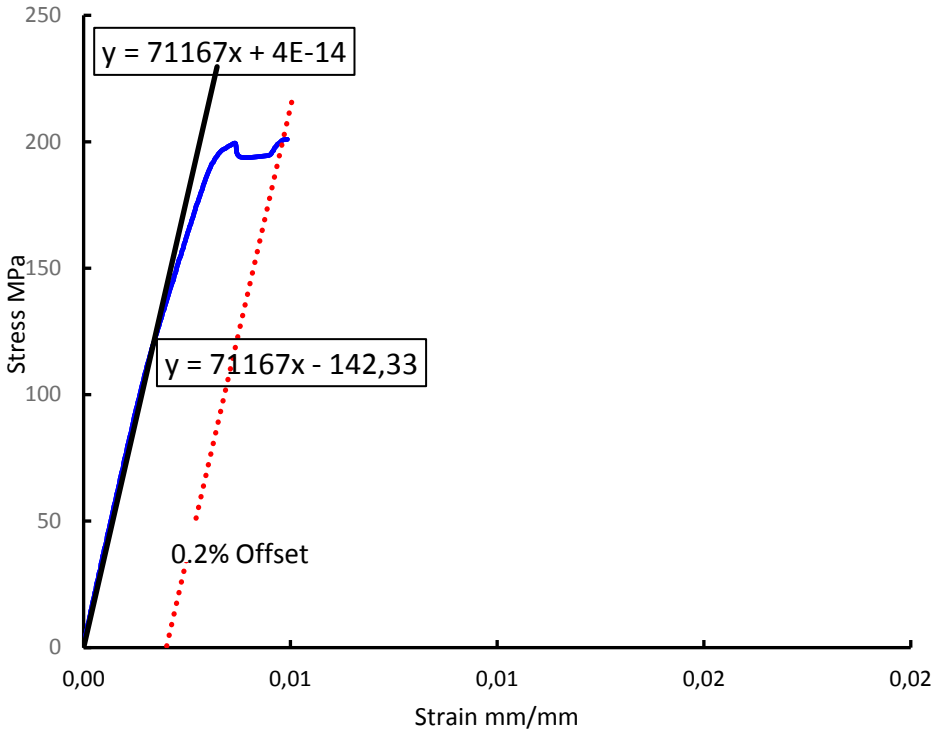

Figure 46: Elastic Region of HAM Specimen (T_HAM3-Longitudinal)

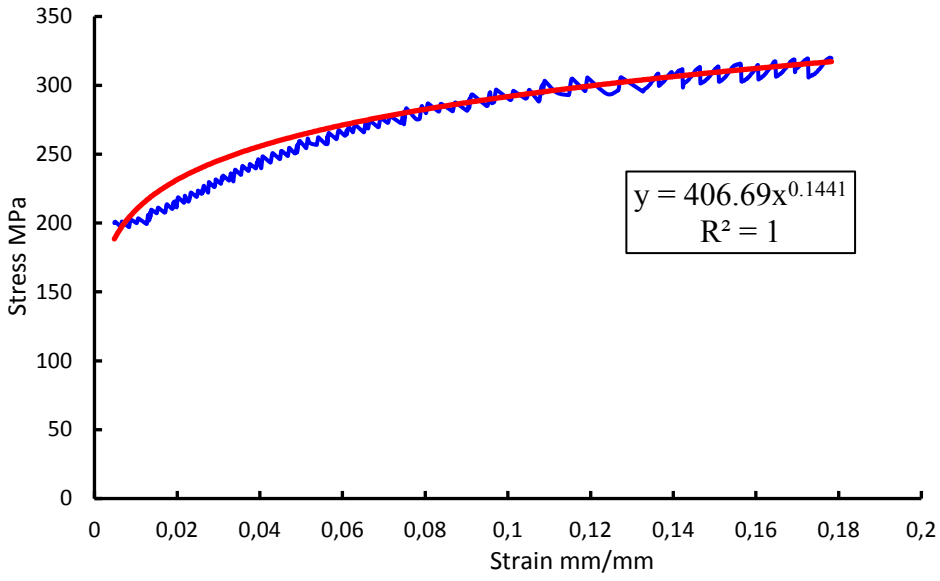

Figure 47: Plastic Region of HAM Specimen (T_HAM3-Longitudinal)

Figure **47** shows the plastic region of specimen T_HAM3. Its toughness or energy can be estimated by computing the area bounded by the fitted curve (red curve).

6.2.1 Results for AA5183 Al alloy Under Tensile Loading

Figure **48** shows a clear relationship between the two samples with respect to the specimens. As can be observed from the figure, the ductility and UTS of T_HAM3 were higher than other specimens due to FSP along the weld deposition path or longitudinal direction.

Table 9: Summary of Mechanical Properties of Specimens under Tensile Loading

Material	Plate thickness (mm)	Modulus of Elasticity (GPa)	Ultimate Tensile Strength (MPa)	Yield Strength (MPa)	Ductility (%)	Toughness/ Energy (J/mm3)
Sample 2						
T_MIG1	6	71.2	333	147	19.4	14.4
T_MIG2	6	71.2	330	147	19.6	14.4
T_MIG3	6	71.2	330	147	18.4	14.2
T_MIG4	6	71.2	334	147	19.2	14.2
T_MIG5	6	71.2	325	147	17	14.4
Sample 1						
T_HAM1	6	71.2	207	167	4	15.4
T_HAM2	6	70.2	300	194	7.3	17.8
T_HAM3	6	71.2	419	194	25.7	76.3

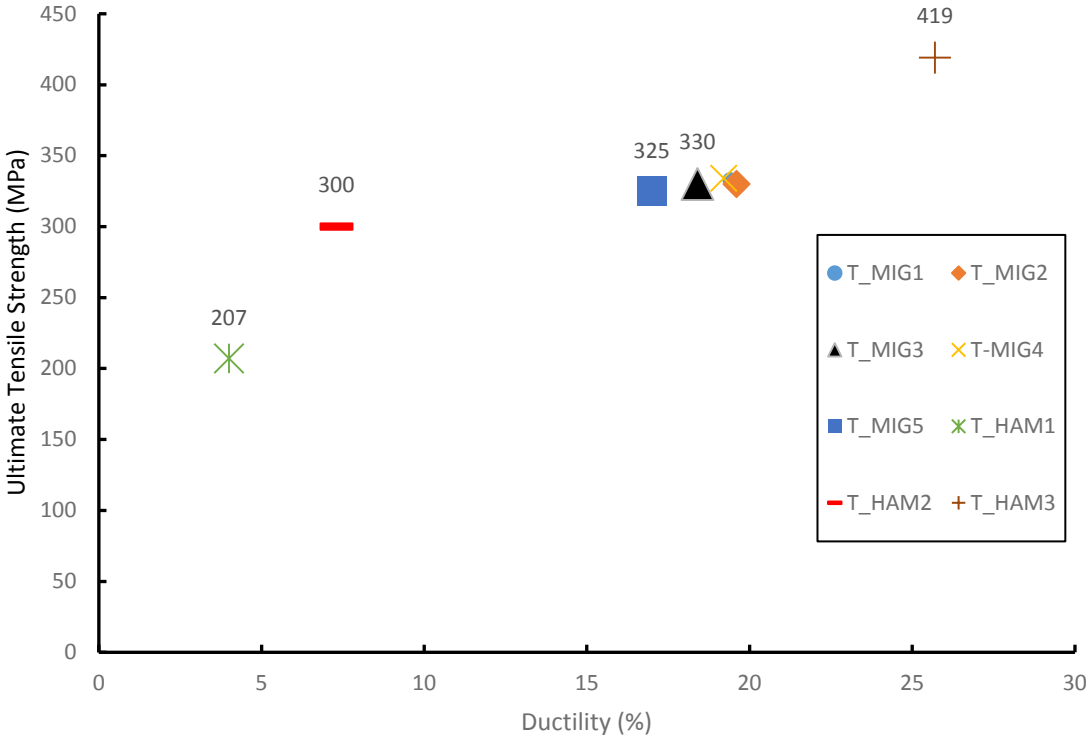

Figure 48: Relationship between the UTS and Ductility of Sample 1 and 2

6.2.2 Global efficiency analysis: GETS

The quality of the sample can thus be assessed by grouping the properties and computing global equivalent coefficients for the overall mechanical properties; that is, the summation of the ratio of individual mechanical property for FSP component (sample 1) to that of base material (sample 2). For tensile test specimens, the Global Efficiency Tensile Strength (GETS) was evaluated based on three design criteria, which comprise of elastic design, plastic design and ductile design.

Mathematically,

$$GETS = CE\frac{E_{FSP}}{E_{BM}} + C\sigma_y\frac{\sigma_{y\_FSP}}{\sigma_{y\_BM}} + C\sigma_{UTS}\frac{\sigma_{UTS\_FSP}}{\sigma_{UTS\_BM}} + CA\frac{A_{FSP}}{A_{BM}} + CU_T\frac{U_{T\_FSP}}{U_{T\_BM}} \quad (18)$$

$Where, E = young\ modulus, \sigma_y = yield\ strength,$

$\sigma_{UTS} = Ultimate\ tensile\ strength, A = Elongation,$

$U_T = Tensile\ Toughness,$

$CE, C\sigma_y, C\sigma_{UTS}, CA, CU_T\ are\ constants\ with\ values\ based\ on\ the\ application.$

Table 10: GETS formulation

	Elastic Design	**Plastic Design**	**Ductile Design**
Young Modulus Coeff. (CE)	0.3	0.1	0.1
Yield Strength Coeff. (Cσ_y)	0.4	0.1	0.15
UTS coeff. (Cσ_UTS)	0.1	0.4	0.15
Elongation coeff. (CA)	0.1	0.2	0.3
Toughness coeff. (CU_T)	0.1	0.2	0.3
GETS_longitudinal (T_HAM3/T_MIG2)	1.62E+00	2.07E+00	2.49E+00
GETS_transverse (T_HAM2/T_MIG5)	1.06E+00	9.27E-01	9.26E-01

Table **10** shows the computed value of GETS in both longitudinal and transversal direction of sample. With the high value of GETS along the longitudinal direction, it can be deduced that this HAM process is highly suitable for manufacturing components that are subject to high tensile loading; that is, manufacturing components with higher elastic, plastic, or ductile property.

6.4 Bending behavior

Figure **49** shows a force-displacement curve for four bending test specimens. From the figure, it can be observed that the maximum load sustained by sample 1 are higher than those of sample 2. This can again be attributed to grain refinement (grain size reduction and removal of numerous voids) and initiation of numerous dislocations, as material flow from advancing side to retreating side during FSP.

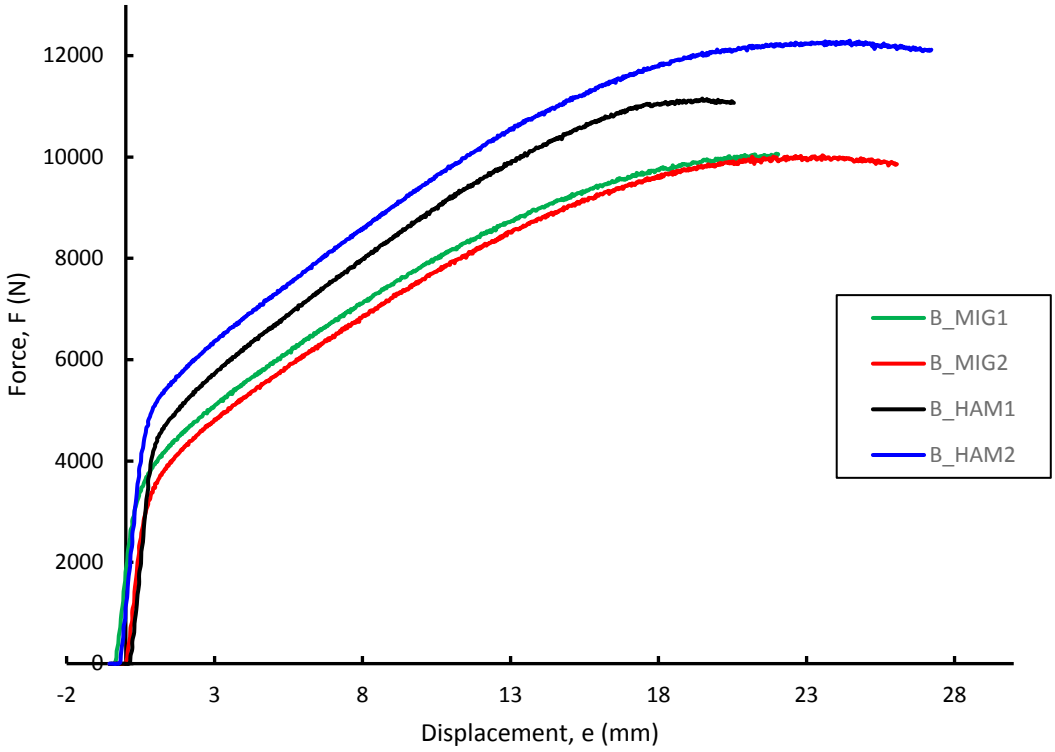

Figure 49: Static bending test on specimens from Sample 1 and 2

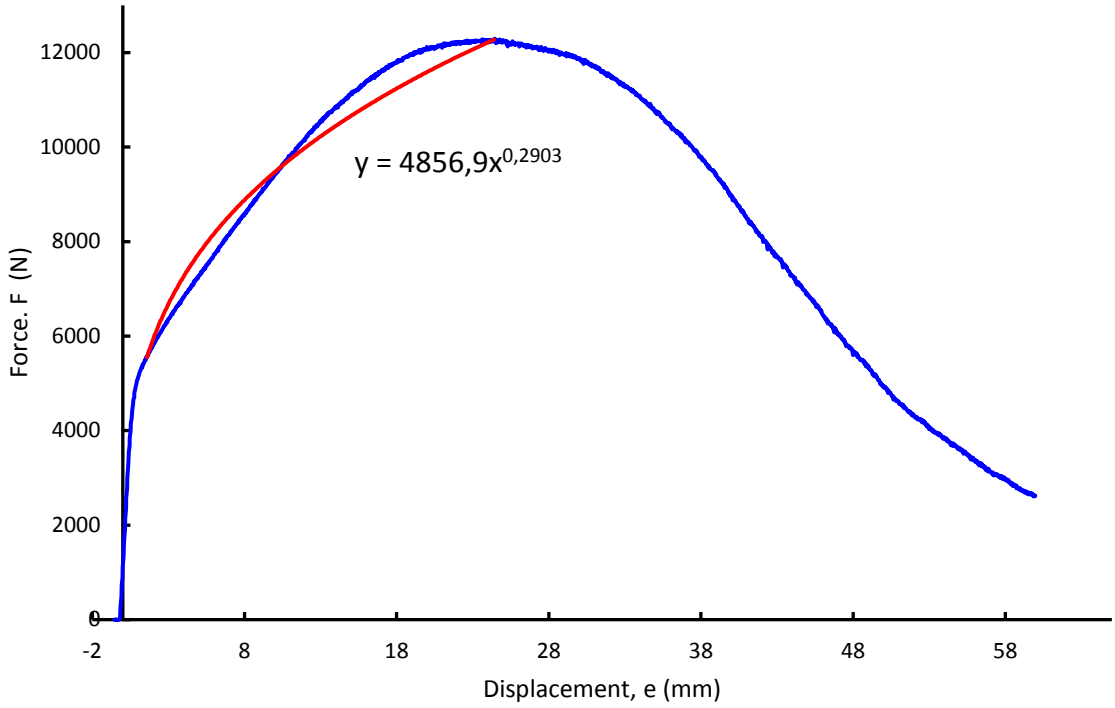

Figure 50: Curve fitted function on B_HAM2 specimen

Figure **50** shows the plastic region of specimen B_HAM2. Its toughness or energy can be estimated by computing the area bounded by the fitted curve (red curve).

$$Energy, U_B = \int_{x_0}^{x_m} Area\ of\ plastic\ region = \int_{x_0}^{x_m} (4856.9x^{0.2903})dx$$

$$U_B = \left[\frac{4856.9x^{1.2903}}{1.2903}\right]_{x_0}^{x_m}$$

$$where, x = displacement\ (mm), x_m = displacement\ at\ maximum\ load$$

6.3.1 Results for AA5183 Al alloy Under Bending Test

A summary of the bending test result in Table **11** shows an improvement on the bending strength (with respect to the max. load) and toughness of *B_HAM1* and *B_HAM2*, in

comparison to *B_MIG1* and *B_MIG2*. These differences can be again attributed to the grain refinement after FSP of sample 1.

Table 11: Summary of static bending test analysis

Material	Plate thickness (mm)	Maximum Load (N)	Displacement at max. Load (mm)	Toughness/ Energy (J)
Sample 2				
B_MIG1	8	10040.92	21.56	164.6905
B_MIG2	8	10006.488	22.338362	166.15161
Sample 1				
B_HAM1	8	11077.346	20.858126	176.075528
B_HAM2	8	12279	24.400368	232.1806

6.3.2 Global efficiency analysis: GEB

The quality of the sample can also be assessed by evaluating Global Efficiency Bending for the bending test. It is the summation of the ratio of individual mechanical property for FSP (sample 1) component to that of base material (sample 2), by using the bending test data. For bending test specimens, the Global Efficiency Bending (GEB) was also evaluated based on three design criteria that comprise of elastic, plastic, and ductile design.

Mathematically,

$$GEB = CF\frac{F_{B\_HAM}}{F_{B\_MIG}} + Ce\frac{e_{HAM}}{e_{MIG}} + CU_B\frac{U_{B\_HAM}}{U_{B\_MIG}} \quad (19)$$

$Where$:

$e = Bending\ displacement,$

$U_B = Bending\ Toughnes$

$F_B = Bending\ force,$

$CF, Ce, and\ CU_B\ are\ constants\ with\ values\ based\ on\ the\ engineering\ applications.$

Table 12: GEB formulation

	Elastic Design	**Plastic Design**	**Ductile Design**
Max. Force coeff. (CF)	0.5	0.4	0.4
Displacement coeff. (Ce)	0.3	0.3	0.15
Bending Toughness coeff. (CU_B)	0.2	0.3	0.45
GEB_longitudinal (*B_HAM2*/*B_MIG2*)	1.22072	1.2377	1.2835
GEB_longitudinal (*B_HAM1*/*B_MIG1*)	1.05557	1.0521	1.0674

Table **12** shows the computed values of GEB in longitudinal direction of samples. With the values of GEB slightly greater than 1 in all 3 kinds of design, it can be deduced that this HAM process is reasonably suitable for manufacturing components that can support relatively high bending loads.

7 Final Remarks

This chapter reviews the previous chapters and provides a roadmap for further development of this hybrid additive manufacturing process.

This whole thesis has been a proof of concept to illustrate that the strength of parts produced by MIG AM can be improved by integrating FSP techniques into the building process. In general, the mechanical properties of the HAM specimens improved significantly in comparison to the MIG AM specimens

The HAM results show maximum UTS of 419 MPa, yield strength of 194 MPa, elongation of 25.7%, toughness of 76.3 J/mm^3, and refined grain microstructure in comparison to the MIG AM with maximum UTS of 334 MPa, yield strength of 147 MPa, elongation of 19.2%, and toughness of 14.2 J/mm^3 under tensile test. As such, there is definitely prospect in this HAM process. However, the extent to which these mechanical properties can be improved will be dependent on future work in further experimentation and modeling of processing parameters. As earlier mentioned that the strength of the manufactured part depends on the values of the MIG welding and FSP parameters and each of the parameters/variables were kept constant during this work. Constant process parameters were used for the two samples and these are based on series of experimental work previously collated. Since the process is quite novel, no standard processing parameters were found on research papers, specifically for the AA5183 aluminium alloy; hence, the manufacturing relied fully on experimental approach.

It was observed that the HAM specimens in transverse direction failed earlier than expected during tensile and bending test, which could possibly attributed to insufficient overlap during multi-passes of FSP and other defects.

Furthermore, an average Vickers hardness value of 95 HV was recorded for the HAM sample and 80.5 HV for the MIG AM sample. That is, the average Vickers hardness of the MIG AM sample (sample 1) is 80.5 HV before FSP and 95 HV after FSP, which shows an improvement in hardness.

Concisely, the most significant conclusions on the developmental process, observations, and application can be summarized as follows:

7.1 Conclusions

1. Guidelines and mathematical algorithm were established for producing components from multi-pass and multi-layer MIG welding deposition.
2. Large components with high strength can be produced at a faster rate using this HAM process in comparison with other additive manufacturing processes.
3. Components free of micro-voids can readily be produce using this HAM process. An application is in the manufacturing of engine blocks for automotive industry.
4. The high values of GETS and GEB indicate that the HAM process can be used in manufacturing parts with high elastic, plastic, and ductile properties.
5. The mechanical properties of 5XXX series aluminium alloy components can be significantly improved by manufacturing them with this HAM process.

7.2 Future developments

- Robotic MIG and FSP HAM:
    - Fatigue, EBSD and SEM analysis should be carried out to further validate the improved performance index of produced samples.
    - Integration of slicing software program for generating STL files from CAD programs that is needed to implement the HAM process for manufacturing industrial grade components should be implemented.
- Optimization of processing parameters using modeling and simulation. The present work used constant values for the processing parameters, which were not necessarily the optimum values. As such, the mechanical properties can be further improved if the optimum values of processing parameters are known and implemented.
- Robotic MIG and friction surfacing HAM
    - This process is similar to the present work, but combines MIG welding with friction surfacing for manufacturing parts. It involves depositing beads on one layer and friction surfacing the undulating surface of the previous layer with a consumable rod, thereby flattening the surface as well as refining the grains

of the welded beads. This process should be properly investigated using similar procedure as with the robotic MIG and FSP hybrid additive manufacturing process.

REFERENCE

[1] W. Terry and G. Tim, "History of additive manufacturing," pp. 1-34, 2014.

[2] Ideas lab staff, "GE Report," 2014. [Online]. Available: http://www.gereports.com/post/93343746148/aviation-proves-newest-territory-for-3d-printing/.

[3] B. Milan, "Laser additive manufacturing: materials, design, technologies, and applications," *Elsevier,* pp. 191-192, 2014.

[4] P. Lequeu, R. Muzzolini, J. Ehrstrom, F. Bron and R. Maziarz, "Slider presentation at the Aeromat Conference," in *Aeromat Conference*, Seattle, WA, 2006.

[5] R. Urbanic, R. Hendrick and C. Burford, "A process planning framework and virtual representation for bead-based additive manufacturing processes," *SpringerLink,* pp. 1-16, 2016.

[6] J. Ruan, T. Sparks, Z. Fan, K. Jacquelyn, P. Ajay and L. Frank, "A review of layer based manufacturing process for metals," Department of mechanical and aerospace engineering, University of Missouri – Rolla., Missouri – Rolla, 2002.

[7] "ASM Handbook, Properties and Selection: Nonferrous Alloys and Special-Purpose Materials," 10th ed., vol. 2, Ohio, ASM International, Materials Park, 1990, pp. 62-122.

[8] Inovar communications Ltd, "http://www.metal-am.com/introduction-to-metal-additive-manufacturing-and-3d-printing/metal-additive-manufacturing-processes/," 12 September 2016. [Online]. Available: http://www.metal-am.com.

[9] S. Palanivel, H. Sidhar and R. Mishra, "Friction stir additive manufacturing: route to high structural performance," *SpringerLink,* vol. 67, no. 3, pp. 616-621, 2015.

[10] S. P. and R. M. S., "Building without melting: a short review of friction-based additive manufacturing techniques," *Int. J. Additive and Subtractive Materials Manufacturing,* vol. 1, pp. 8-13, 2017.

[11] V. Pedro and T. Wayne, "State of the art in friction stir welding," *Springer-Verlag Berlin Heidelberg,* pp. 12-14, 2011.

[12] S. Rajiv and S. Partha, "Influence on mechnical properties," in *Friction stir welding and processing*, Springer, 2014, pp. 282-283.

[13] G. Joao, "Development of friction surfacing for engineering application," Instituto superior tecnico, 2013.

[14] J. Sharma and S. Simhambhatla, "Additiove manufacturing of complex shapes through weld-deposition and feature based slicing," *ACME,* 2015.

[15] J. Y. Jeng and M. C. Lin, "Mold fabrication and modification using hybrid processes of selective laser cladding and milling," *ScienceDirect,* vol. 110, no. 1, pp. 98-103, 2001.

[16] O. JPaul, P. Paul, S. Rossi, H. Gareth and J. Nick, "Meta-based additive layer manufacturing: variation, correlations and process control," *ScienceDirect,* pp. 583-610, 2016.

[17] R. Mahamood and E. Akinlabi, "Laser metal deposition of functionally graded Ti6Al4V/TiC," *ScienceDirect,* vol. 84, pp. 402-410, 2015.

[18] Y. Zhi-peng, Z. Zhi-jing, J. Xin, X. Mu-Zheng and S. Jiang-zhou, "Study of hybrid additive manufacturing based on pulse laser wire depositing and milling," *SpringerLink,* pp. 1-12, 2016.

[19] Matsuura, "Unique one process solution: laser sintering and milling," Matsuura, 2015. [Online]. Available: http://www.matsuura.co.jp/english/contents/products/new-lumex03.html. [Accessed 12 November 2016].

[20] Z. Bingjing, W. Hong, Y. Rongzeng, W. Chao, N. Yu and H. Min, "Properties evaluation of a Ti-6Al-4V alloy scaffold fabricated by electron beam melting and selective laser melting for bone tissue engineering," *Ingenta,* vol. 6, no. 10, pp. 832-842, 2016.

[21] L. Wei, L. Jie, Z. Yan, L. Shuai, W. Shifeng, W. Qingsong, Y. Chunze and S. Yusheng, "Effect of laser scanning speed on a Ti-45Al-2Cr-5Nb alloy processed by selective laser melting: Microstructure, phase and mechanical properties," *Infona,* pp. 626-636, 2016.

[22] H. Takagi, T. Abe, H. Sannomiya, S. Nishiyama, S. Ohta and Y. Nakamu, "Strength of laminated object of magnesium alloy fabricated by direct metal lamination using arc discharge," in *8th international conference on leading edge manufacturing in 21st century*, Kyoto Research Park, Kyoto, Japan, 2015.

[23] K. Kassmaul, F. Schoch and H. Lucknow, "High quality large components shape welded by a SAW process," *Weld Journal,* 1983.

[24] M. McAninch and C. Conrardy, "Shape melting- a unique near-net shape manufacturing process," *WeldRevInt,* vol. 10, no. 1, pp. 33-40, 1991.

[25] T. Doyle, D. Edmonds and M. McAninch, "Method and apparatus for building a workpiece by deposited welding". United States of America Patent 482186, 1988.

[26] S. Yong-Ak, P. Sehyung and C. Soo-Won, "3D welding and milling: part II—optimization of the 3D welding process using an experimental design approach," *ScienceDirect,* vol. 45, no. 9, p. 1063–1069, 2005.

[27] S. Yong-Ak, P. Sehyung, C. Doosun and J. Haesung, "3D welding and milling: Part I–a direct approach for freeform fabrication of metallic prototypes," *ScienceDirect,* vol. 45, no. 9, p. 1057–1062, 2005.

[28] C. Yong, L. Sheng and W. Wanglong, "Overlapping model of beads and curve fitting of bead section for rapid manufacturing by robotic MAG welding process," *Elsevier,* 2010.

[29] Y. Cao, S. Zhu, T. Wang and W. Wang, "Modeling of welded bead profile for rapid prototyping by robotic MAG welding," *Scopus,* 2009.

[30] H. Ghazvinloo, A. Honarbakhsh-Raouf and N. Shadfar, "Study on mechanical properties and penetration of MAG weld," *Scopus,* 2009.

[31] X. Yang, Z. Haiou and Z. Fei, "Improvement in geometrical accuracy and mechanical property for arc-based additive manufacturing using metamorphic rolling mechanism," *ASME,* vol. 138, no. 11, 2010.

[32] P. K. Palani and N. Murugan, "Development of Mathematical Models for Prediction of Weld Bead Geometry in Cladding by Flux Cored Arc Welding," *SpringerLink,* vol. 30, no. 7, pp. 669-676, 2006.

[33] S. ,. K. K. P. Suryakumar, A. Bernard, U. Chandrasekhar, N. Raghavender and D. Sharma, "Weld bead modeling and process optimization in Hybrid Layered Manufacturing," *ScienceDirect,* vol. 43, no. 4, p. 331–344, 2011.

[34] Z. Xiangman, Z. Haiou, W. Guilan, B. Xingwang, F. Youheng and Z. Jingyi, "Simulation of microstructure evolution during hybrid deposition and micro-rolling process," *SpringerLink,* vol. 51, no. 4, pp. 6735-6749, 2016.

[35] P. A. Colegrove, H. E. Coules, J. Fairman, F. Martina, T. Kashoob, H. Mamash and L. D. Cozzolino, "Microstructure and residual stress improvement in wire and arc additively manufactured parts through high-pressure rolling," *ScienceDirect,* vol. 213, no. 10, pp. 1782-1791, 2013.

[36] Y. Song and S. Park, "Experimental investigations into rapid prototyping of composites by novel hybrid deposition process," vol. 171, no. 1, pp. 35-40, 2006.

[37] I. Gibson, D. Rosen and B. Stucker, "Additive manufacturing technologies: rapid prototyping to direct digital manufacturing," *SpringerLink,* 2010.

[38] J. Liu and A. To, "Topology optimization for hybrid additive-subtractive manufacturing," *SpringerLink,* pp. 1-19, 2016.

[39] S. Rajiv and S. Partha, Friction stir welding and processing, Springer, 2014.

[40] Z. Y. Ma, "Friction stir processing technology: A review," *SpringerLink,* vol. 39, no. 3, p. 642–658, 2008.

[41] C. H. Chuang, J. C. Huang and P. J. Hsieh, "Using friction stir processing to fabricate MgAlZn intermetallic alloys," *ScienceDirect,* vol. 53, no. 12, p. 1455–1460, 2005.

[42] L. Ceschinia, I. Boromeia, G. G. Minakb, A. Morria and F. Tarterinia, "Effect of friction stir welding on microstructure, tensile and fatigue properties of the AA7005/10 vol.%Al2O3p composite," *ScienceDirect,* vol. 67, no. 3-4, pp. 605-615, 2007.

[43] J. Q. N. T. ,. M. R. Su and M. Mahoney, "Microstructural investigation of friction stir welded 7050-T651 aluminium," *ScienceDirect,* vol. 51, p. 713–729, 2003.

[44] P. Cavaliere and P. ,. De Marco, "Effect of friction stir processing on mechanical and microstructural properties of AM60B Magnesium alloy," *SpringerLink,* vol. 41, no. 11, p. 3459–3464, 2006.

[45] T. R. McNelley and M. McMahon, "Microtexture and grain boundary evolution during microstructural refinement processes," *SpringerLink,* vol. 28, no. 9, p. 1879–1887, 1997.

[46] ESAB, "ESAB," ESAB, 2016. [Online]. Available: http://www.esabna.com/us/en/products/index.cfm?fuseaction=home.product&productCode=10905&tab=2. [Accessed 27 January 2017].

[47] ESAB, "ESAB," 2016. [Online]. Available: http://mam.esab.com/assets/1/BDBA5CC688D14EBE822C00D265DF8E7D/doc/736519DC2B364429B27577DBCBD9FBAA/10905-en_US-FactSheet_Main-01.pdf. [Accessed February 2017].

[48] E. William, "Metal additive manufacturing: a review," *SpringerLink,* pp. 1917-1928, 2014.

[49] J. Baumann, "Technical Report: Production of Energy Efficient Preform Structures.," Huntington Beach, CA, 2012.

[50] J. K.V., M. M.W., R. Mishra, S. S.L. and F. D.P., "Microstructure of FSP zone," in *Friction stir welding and processing*, Indianapolis, USA, TMS, 2001, pp. 219-221.

[51] K. Sindo, Welding metallurgy, 2nd ed., John Wiley and sons, INC., 2003, pp. 208-217.

[52] K. Benyounisa and A. Olabi, "Optimization of different welding processes using statistical and numerical approaches – A reference guide," *ScienceDirect,* vol. 39, no. 6, p. 483–496, 2008.

[53] B. L.P., C. J.D., J. J.S., L. A.R. and F. J.M., "Fatigue life improvement by friction stir processing of 5083 aluminium," *Elsevier,* pp. 68-74, 2014.

[54] R. Silva, G. Barbosa and J. Carvalho, "Additive manufacturing of metal parts by welding," in *International federation of automation and control conference paper*, 2015.

[55] T. Imerito, "Science Spectrum," [Online]. Available: http://science-spectrum.com/additive-manufacturing-adding-creativity-to-engineering/. [Accessed March 2017].

[56] G. Dongdong, D. Donghua, Wenhua, C and H. C, "Selective Laser Melting Additive Manufacturing of Hard-to-Process Tungsten-Based Alloy Parts With Novel Crystalline Growth Morphology and Enhanced Performance," *ASME Digital Collections,* vol. 138, no. 8, pp. 1-11, 2015.

ANNEX

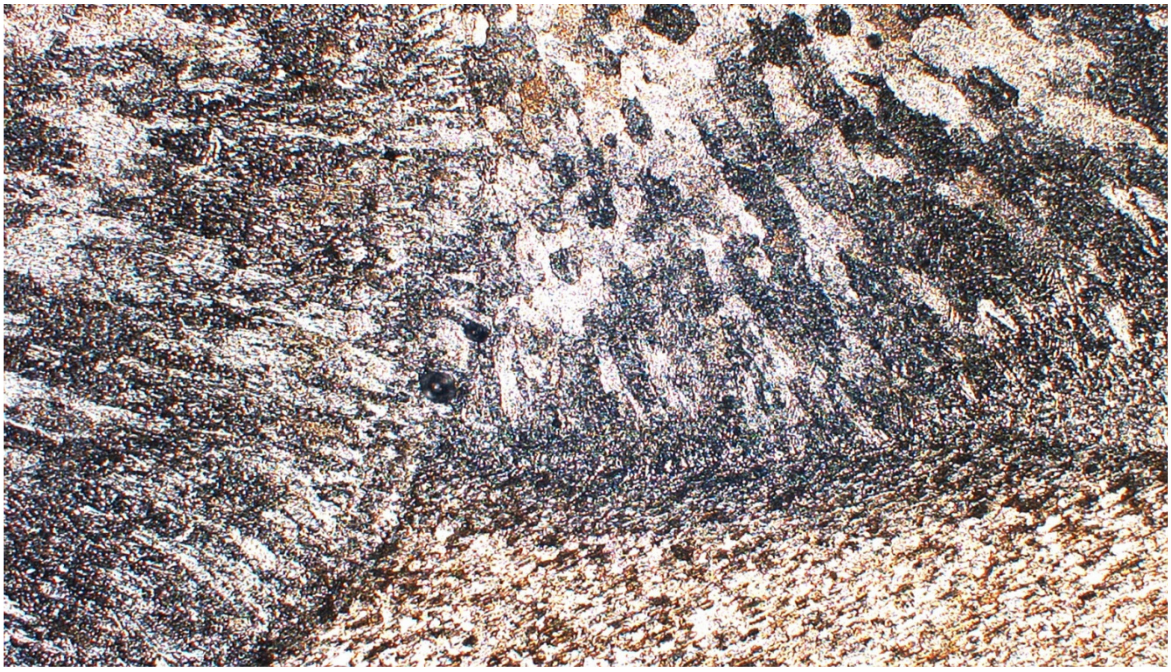

Figure 51: Boundary between base plate and MIG-weld beads under optical microscope

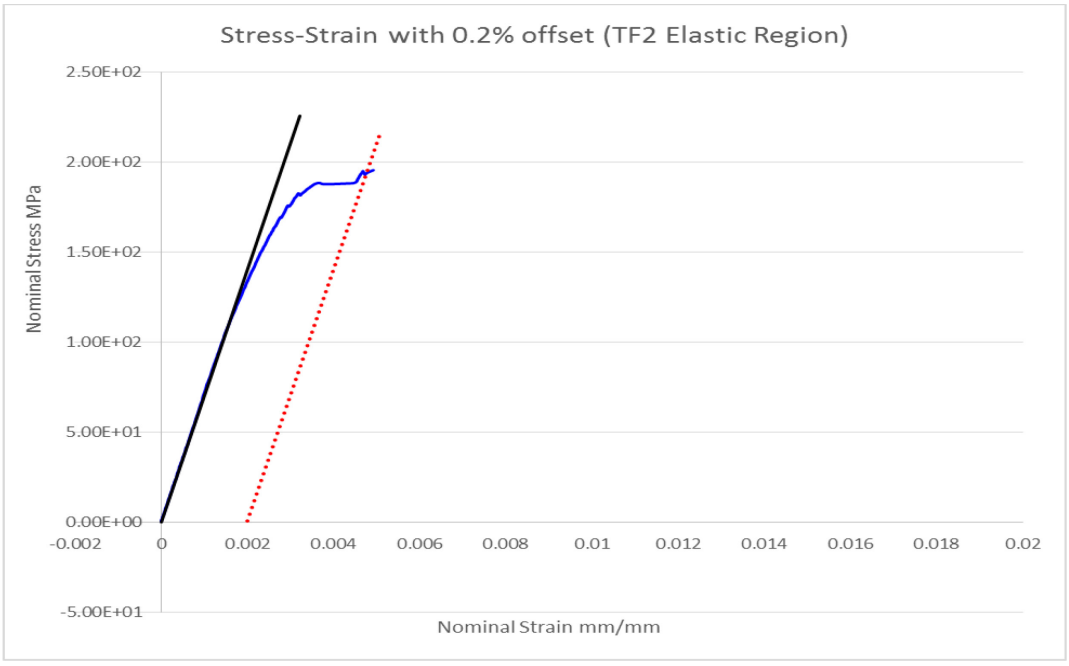

Figure 52: Elastic Region of T_HAM2

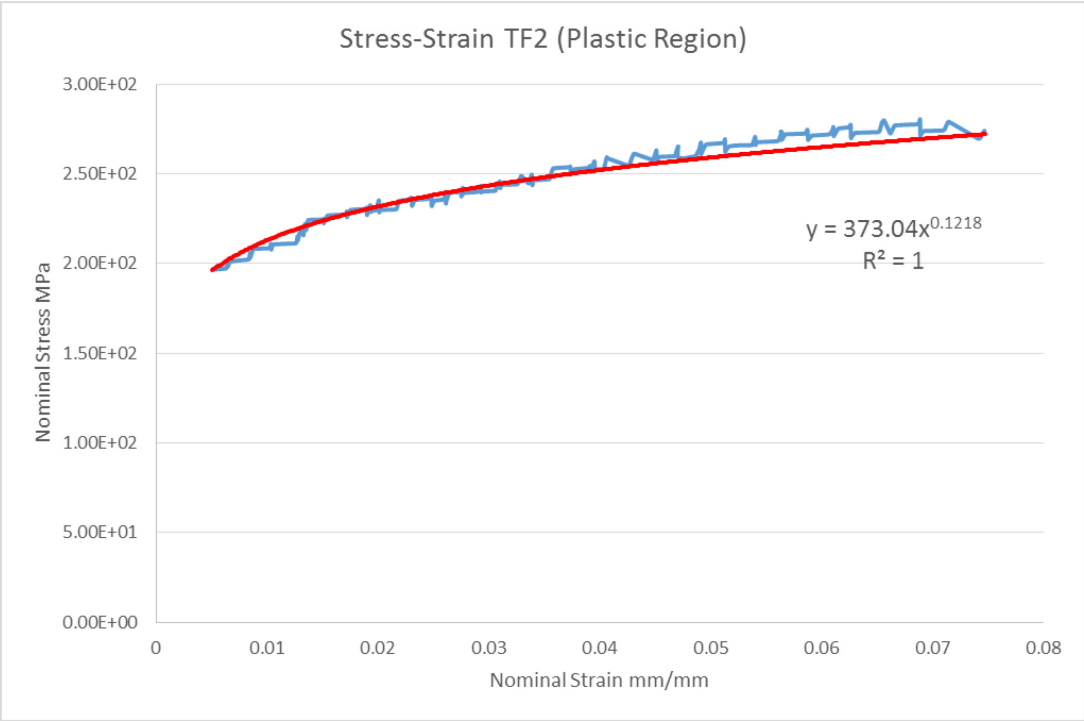

Figure 53: Plastic Region of T_HAM2

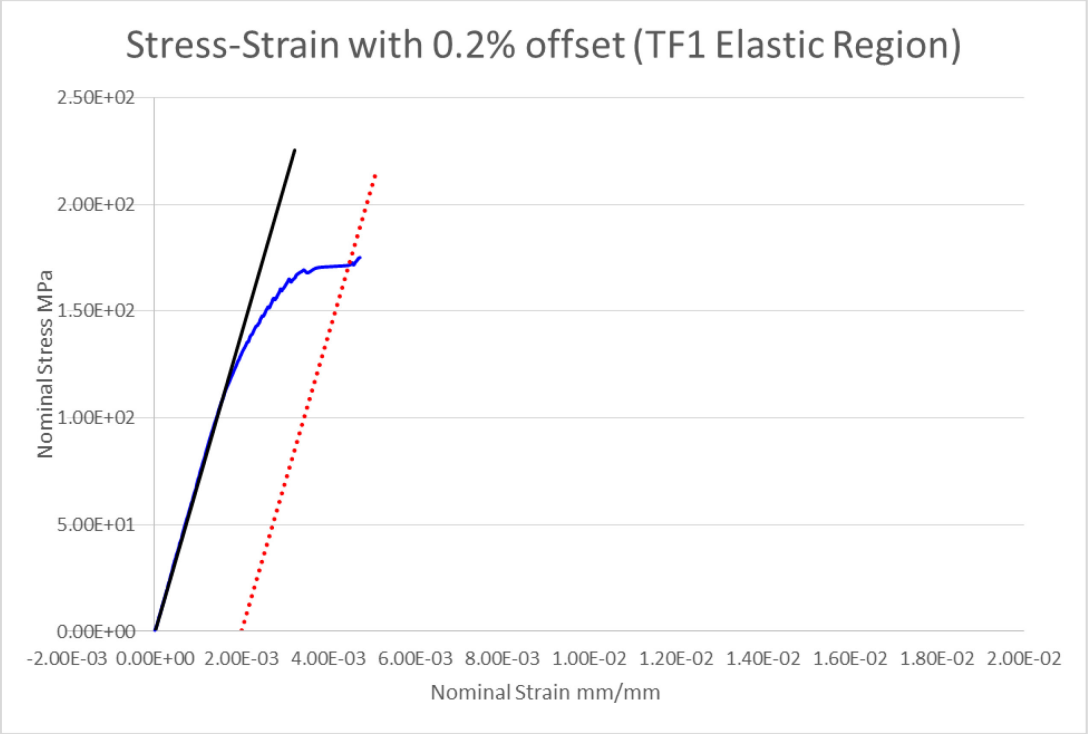

Figure 54: Elastic Region of T_HAM1

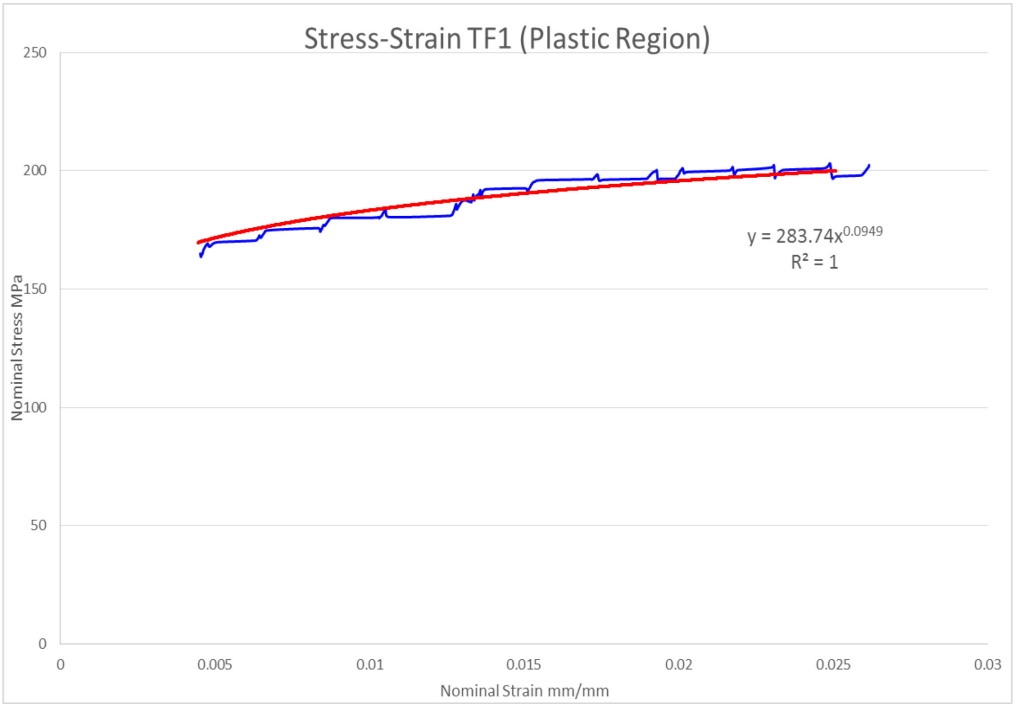

Figure 55: Plastic Region of T_HAM1

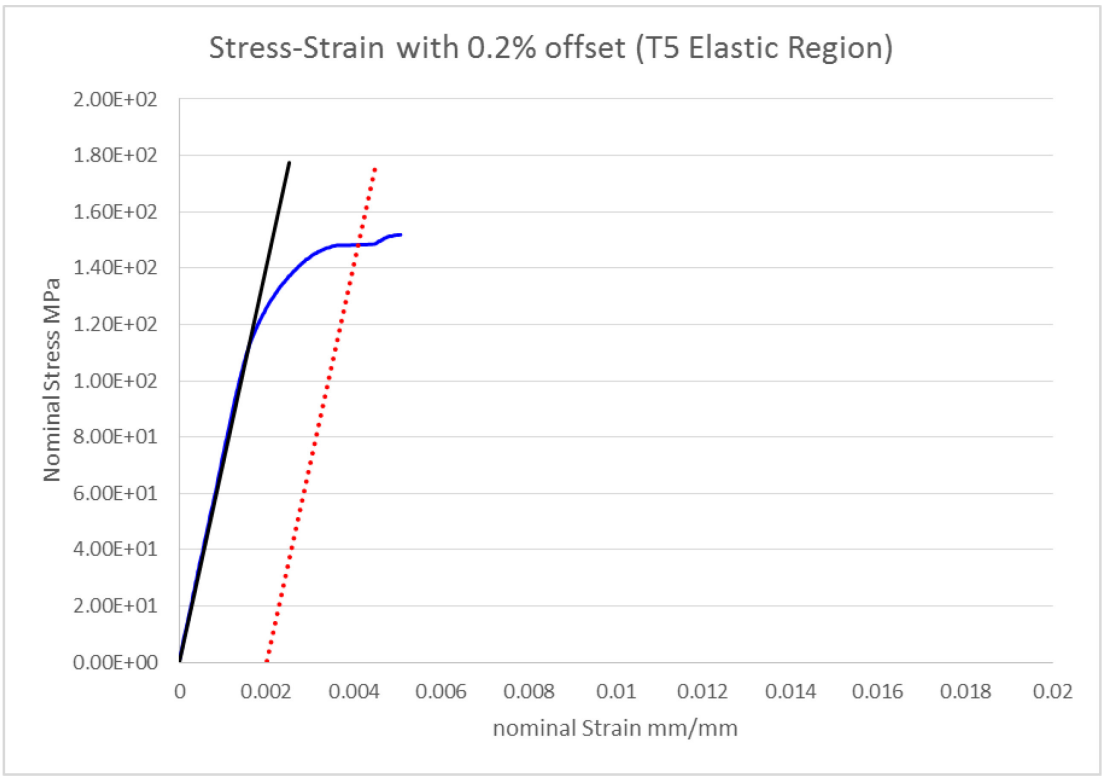

Figure 56: Elastic Region of T_MIG5

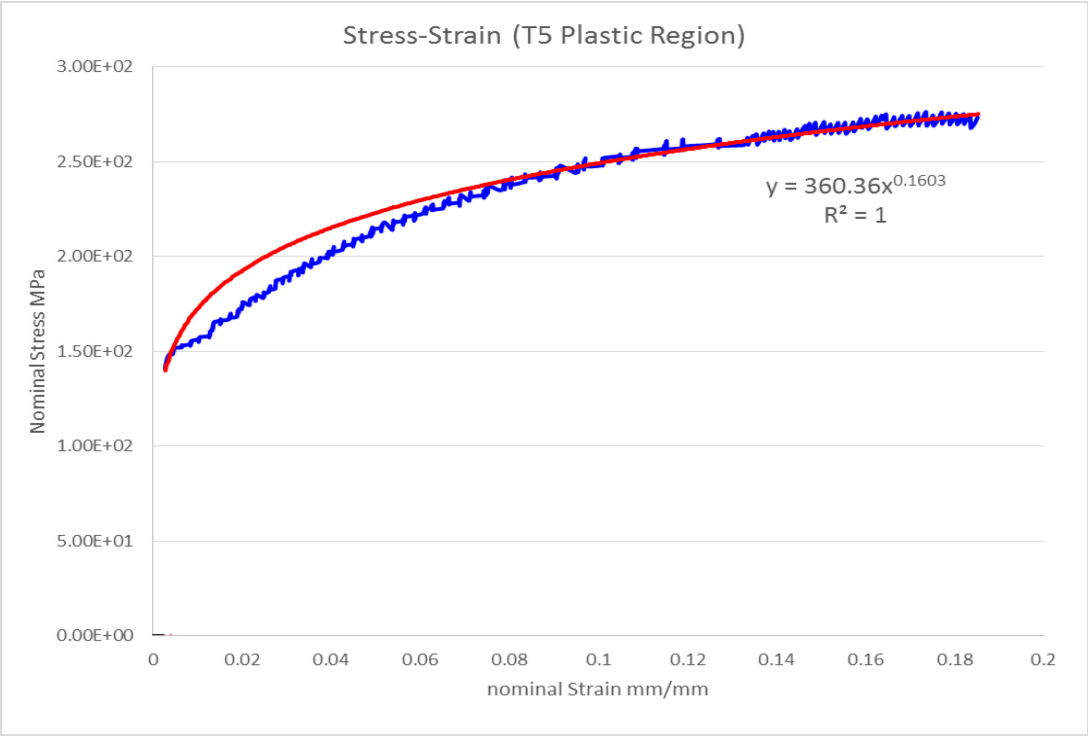

Figure 57: Plastic Region of T_MIG5

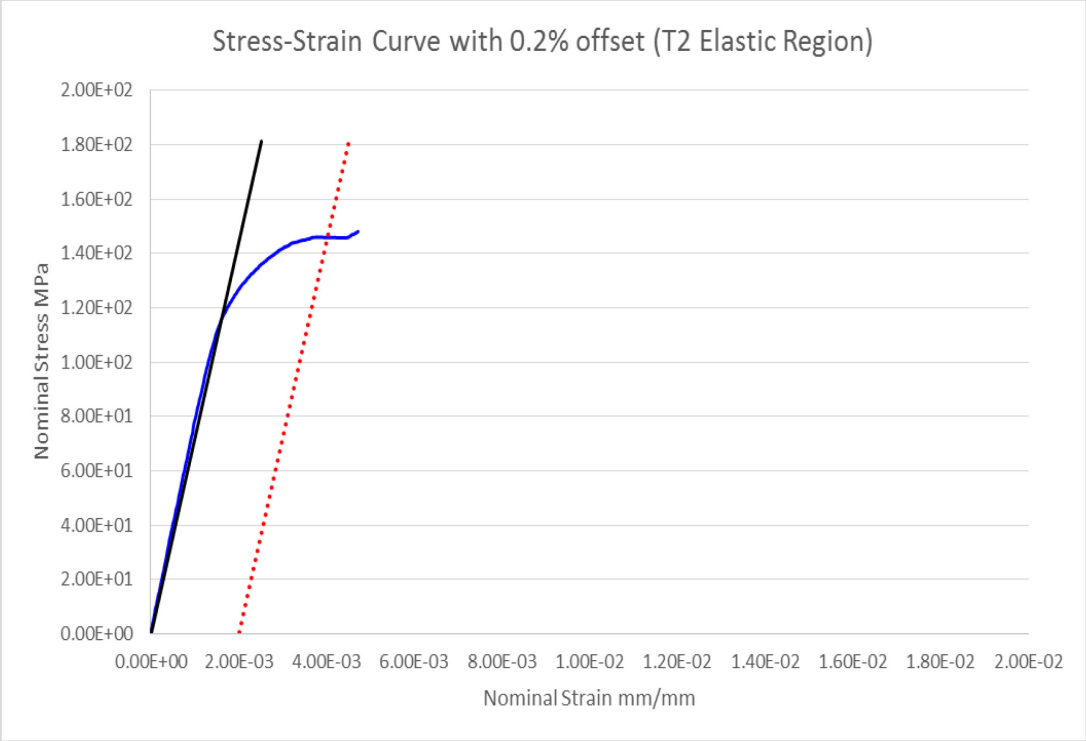

Figure 58: Elastic Region of T_MIG2

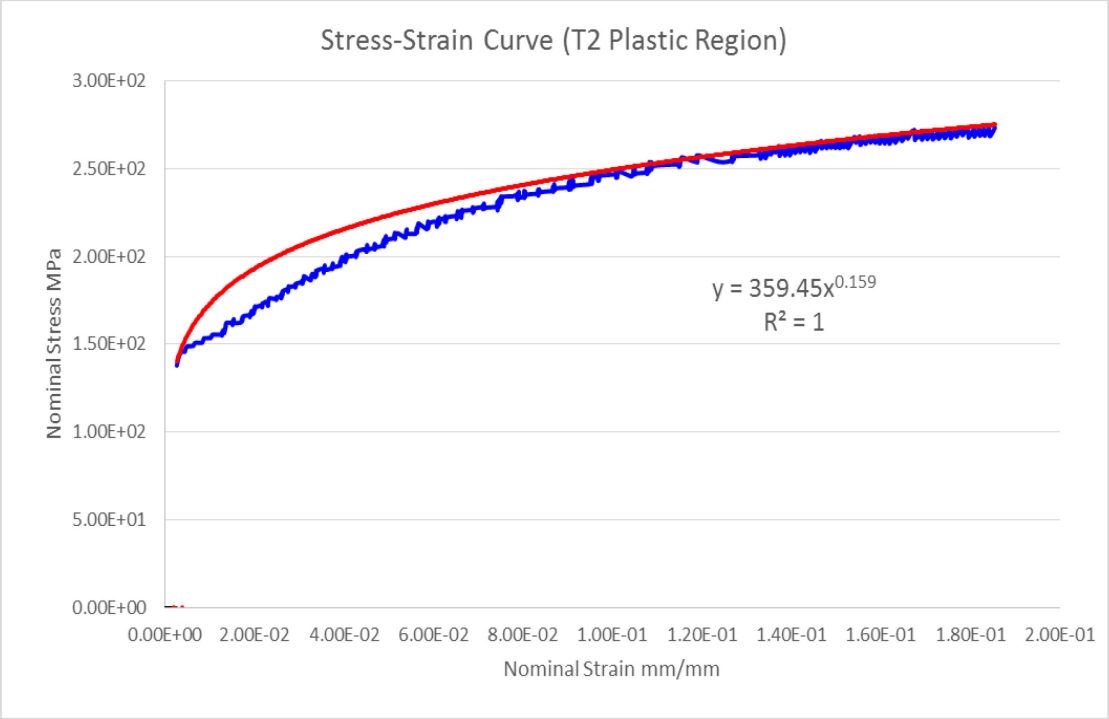

Figure 59: Plastic Region of T_MIG2

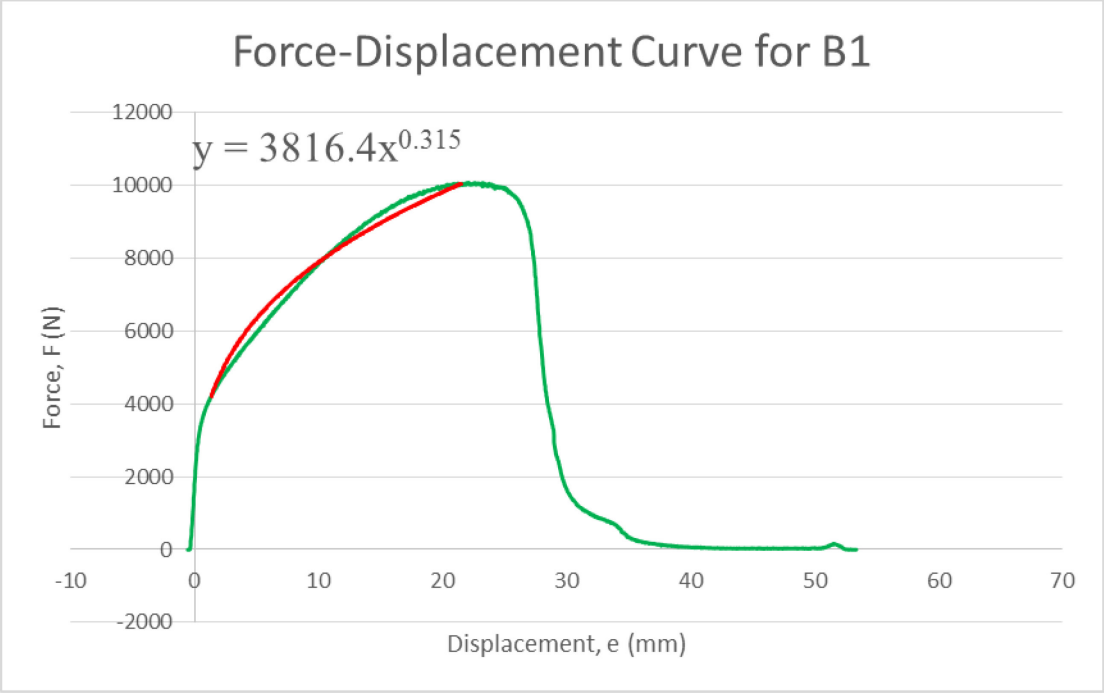

Figure 60: Curve fit function on Force-Displacement of B_MIG1

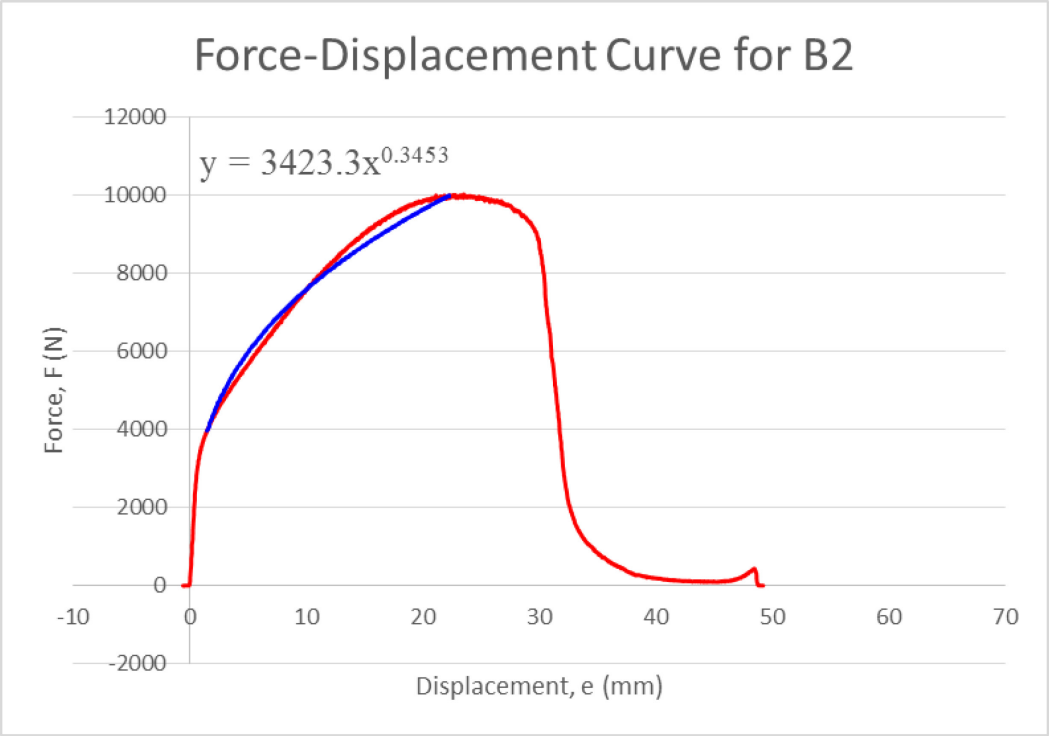

Figure 61: Curve fit function on Force-Displacement of B_MIG2

Ω

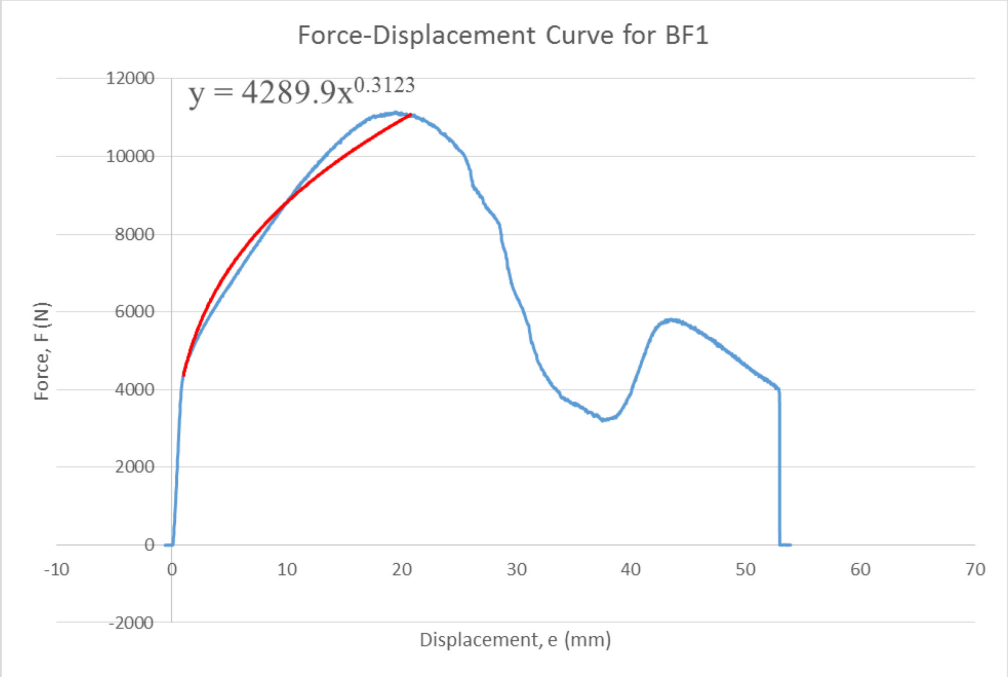

Figure 62: Curve fit function on Force-Displacement of B_HAM1